LUNFD6/(NFFL-7140) 1997

Physics Analysis in HERA-B

&

Beauty Production at the HERA-B Experiment

&

Pion and Electron Identification in ATLAS using a Module Layout of the Barrel TRT

Jenny Ivarsson [1,2]

May 5, 1997

Thesis for the degree of filosofie licentiat.

[1]University of Lund, Institute of Physics, BOX 118, S - 221 00 Lund, Sweden.
[2]http://www.quark.lu.se/~ jenny

Abstract

The technical challenges of the HERA-B and ATLAS experiments are in many aspects similar. This thesis includes a presentation of the two experiments and a study on the feasibility of physics analysis within HERA-B. Emphasis is put on $B_d \to J/\psi K_S^0$ reconstruction efficiencies.

Contents

1 Preface **3**

2 The ATLAS Experiment **5**
2.1 Introduction 5
2.2 Requirements 6
2.3 Detector Design 6
2.4 Trigger 9

3 The HERA-B Experiment **11**
3.1 Introduction 11
3.2 Requirements 13
3.3 Detector Design 13
3.4 Trigger 16

4 Transition Radiation Detectors **18**
4.1 Introduction 18
4.2 Transition Radiation 18
4.3 The ATLAS TRT 22
4.4 The HERA-B TRD 29

5 B Physics and CP Violation **30**
5.1 Introduction 30
5.2 Heavy Quark Symmetry 30
5.3 B_c Mesons 33
5.4 CP Violation 34

6 The $b\bar{b}$ Cross Section at HERA-B **41**
6.1 Introduction 41
6.2 Nuclear Dependence 42
6.3 Feynman's x Distribution 42
6.4 Summary 43

7 Analysis in HERA-B **45**
7.1 Introduction 45
7.2 HERA-B Software 45
7.3 The Golden Channel 48

8 Conclusion **60**

A $B^0 - \bar{B}^0$ mixing **61**

Chapter 1

Preface

ATLAS and HERA-B are two high energy physics experiments under construction at two different laboratories in Europe. ATLAS is a general-purpose detector planned at the Large Hadron Collider (LHC) at CERN in Geneva. The center of mass energy in the proton anti-proton collider will be 14 TeV allowing for the production of very heavy particles. The extremely high luminosities and high energies are challenging for detector construction. ATLAS is scheduled to take its first data around the year of 2005. During the time, development is continuously going on and experiences are achieved.

The HERA-B experiment at the HERA accelerator in Hamburg is a shorter term experiment, scheduled to take its first data already in 1998. The challenges are however similar to the ATLAS requirement. Meeting the problems already at present time it can in some sense be seen as a test-bench for future constructions. At the same time, HERA-B can profit from developments already made for the LHC detectors. HERA-B is a B factory using only the 820 GeV proton beam of the HERA accelerator and directing the beam halo particles onto target wires. The high luminosities lead to several interactions per bunch crossing and to rates comparable to the LHC scenario.

For the mentioned reasons it is interesting to compare these two experiments. This report is initiated with such an introductory comparison followed by a study on transition radiation detectors which will be used in both experiments.

The aim when going to higher energies is to explore physics at very small distances and eventually find the answers on basic questions. Two of the most important questions are the origin of mass and the asymmetry between matter and antimatter. The former is one of the main motivations for building the ATLAS detector. The latter is closely connected to our sense of direction of time. The physical explanation for it is called CP violation. CP is the simultaneous transformation under charge conjugation and parity.

When CP symmetry is broken matter and antimatter behave differently. The CP violation is a small statistical effect. It can be studied only at very high luminosities in high energy environments, where quark-antiquark composites can be produced. Neutral mesons are a good source for CP violation, since they mix between states and anti-states. CP violation has already been seen in the decay of neutral K-mesons, which have mixtures of the quark contents ($\bar{\mathrm{d}}$ s) and (d $\bar{\mathrm{s}}$). The effect of CP violation is expected to be larger in the system of B mesons where the s-quarks are exchanged by the much heavier b-quarks. For reasons explained in chapter 5 the decay $B^0 \to J/\psi K^0_S$, where the B meson can decay directly or via mixing to $\bar{B}^0$, is particularly interesting and has been labeled the *golden channel*. Finding the asymmetry between the number of $B^0 \to J/\psi K^0_S$ and $\bar{B}^0 \to J/\psi K^0_S$ decays is the main goal of the HERA-B experiment.

A condition for good measurements is a reasonable cross section for B meson production. This is discussed in chapter 6.

The main part of this report deals with analysis tools for the HERA-B experiment and a study on the reconstruction rates for the main channel, which gives a hint on the feasibility to measure CP violation in the B system using the B factory at HERA.

The progress I have made with the analysis program together with insights on the conditions of the HERA-B experiment owe many thanks to Rainer Mankel. No analysis would be possible without reconstruction code programmed by him, Thomas Lohse, Siegmund Nowak, Alexandre Spiridonov and Hartwig Albrecht.

For the interesting part I have taken in the ATLAS experiment I thank, amongst others, Ulrik Egede and of course Torsten Åkesson, my supervisor.

I would like to direct special thanks to Cecilia Jarlskog and Torbjörn Sjöstrand for discussing the physics with me.

My financial support comes from Lund University, Swedish Science Research Council and Svenska Institutet. I also thank Hermann Kolanoski and DESY-IfH in Zeuthen for the generous hospitality.

Chapter 2

The ATLAS Experiment

2.1 Introduction

ATLAS is a general purpose detector at the LHC. One of its challenges is to find the origin of mass. Many other physics studies will be performed like for example top quark physics and CP violation in B decays.

In the Standard Model (SM), the phenomenon responsible for the mass of particles is described by electroweak symmetry breaking. The symmetry is broken by a scalar field with an associated Higgs boson. The mass of the Higgs boson can range from 80 GeV up to 1 TeV or more. Depending on the mass there are five main decay channels to look for:

$$\begin{array}{rcl} 80\ \text{GeV} < m_H < 120\ \text{GeV} & : & \text{H} \rightarrow \text{b}\bar{\text{b}} \\ 90\ \text{GeV} < m_H < 150\ \text{GeV} & : & \text{H} \rightarrow \gamma\gamma \\ 130\ \text{GeV} < m_H < 2m_Z & : & \text{H} \rightarrow \text{ZZ}^* \rightarrow 4\ell \\ m_H > 2m_Z & : & \text{H} \rightarrow \text{ZZ} \rightarrow 4\ell,\ \ 2\ell\nu \\ m_H \sim 1\ \text{TeV} & : & \text{H} \rightarrow \text{WW} \rightarrow \ell\nu jj,\ 2\ell j \end{array}$$

The signatures for interesting events are high p_T electrons, gamma, muons, jets, b-tagging and missing transverse energy. In pp collisions with E_{CMS} = 14 TeV the background of hadrons from QCD interactions is very high. Finding a Higgs signal requires high luminosities.

In LHC the bunch crossing rate is 40 MHz. For an inelastic cross-section of $\sim$ 70 mb, around 23 minimum bias events per bunch crossing are expected at the peak luminosity of $10^{34} cm^{-2} s^{-1}$.

In an initial stage the luminosity will be $10^{33} cm^{-2} s^{-1}$. Physics is then accessible using more complex signatures as tau-lepton detection and heavy flavour tags from secondary vertices and reconstruction of CP eigenstates.

The design of the ATLAS detector is now essentially finalised and pre-

sented in a series of technical design reports. The overview in this chapter is based on the ATLAS Technical Proposal [1].

2.2 Requirements

The variety of final-state signatures puts many demands on the detector design:

- Large acceptance in rapidity coverage.
- Triggering and measurements of particles at low-p_T thresholds.
- Efficient, fine granularity tracking for lepton momentum measurements, b-quark tagging, enhanced electron and photon identification.
- Secondary vertex detection (at the initial luminosity) for heavy flavour reconstruction.
- Very good electromagnetic calorimetry for electron and photon identification and measurements.
- Jet and missing E_T calorimetry.
- Stand-alone, precision, muon-momentum measurements (up to highest luminosity). Very low-p_T trigger capability (at lower luminosity).

To accept new data every 25 ns the readout and processing electronics have to be extremely fast. In the first step of a trigger decision only reduced granularity data from part of the detectors can be used.

Anything that is placed into the very high LHC background has to be radiation hard. The detector parts closest to the beam (inner tracking, end-cap calorimetry) are exposed to several MRad per year, the forward calorimeter as much as 200 MRad. The annual radiation doses on the outer tracking parts are 200-500 kRad per year.

2.3 Detector Design

The ATLAS detector consists essentially of three blocks: the inner detector, the calorimetry and the muon spectrometer. The basic design of the calorimetry and the inner detector is depicted in fig. 2.1.

The inner detector is built up by tracking devices of varying granularity and radiation hardness, depending on the distance from the interaction point. The radius of the inner detector volume is 1.15 m and the length is 6.8 m.

The tracks are bent in a 2T magnetic field of a super-conducting solenoid around the inner volume.

The electromagnetic calorimeter is a highly granular liquid argon sampling calorimeter. It is contained in a cylinder of outer radius 2.25 m and length 13.3 m. In the liquid argon technology, showers develop in lead, which is placed in a liquid argon absorber. The electromagnetic calorimeter shall detect leptonic and semileptonic decays of B mesons, Z and W-bosons, as well as H$\rightarrow \gamma\gamma$ decays. The desired resolution is

$$\frac{\Delta E}{E} = 0.7\% \oplus \frac{10\%}{\sqrt{E}} \tag{2.1}$$

Identification of jets and measurement of total missing transverse energy are performed with the combined electromagnetic and hadronic calorimeter. The barrel part of the hadronic calorimeter is a scintillator tile calorimeter. Its outer radius is 4.25 m and its length 12.2 m. In the scintillator tile technique, the showers develop in iron absorbers and scintillator plates are placed in a novel configuration. An orientation perpendicular to the beams provides a good sampling homogeneity. The emitted light is shifted by the wavelength shifting (WLS) fibers before detection by PM tubes. In the endcap, where the radiation is high, this technique is replaced by Liquid Argon.

A stand-alone muon spectrometer extends out to a radius of 11 m from the interaction point. It consists of a superconducting air-core toroid magnet system with muon chambers. The length of the barrel toroids is 26 m and the distance between the outermost forward muon chambers is 44 m.

Tracking System

The inner detector is divided into a high-resolution part at inner radii (<60cm) and continuous tracking at outer radii.

- To achieve the good momentum and vertex resolution in the very large track density at LHC, very fine granularity detectors are needed at inner radii.

  Around the vertex region semiconductor pixel detectors will be used. To limit material and cost they cover only a small area. They are followed by semiconductor tracking detectors based on silicon.

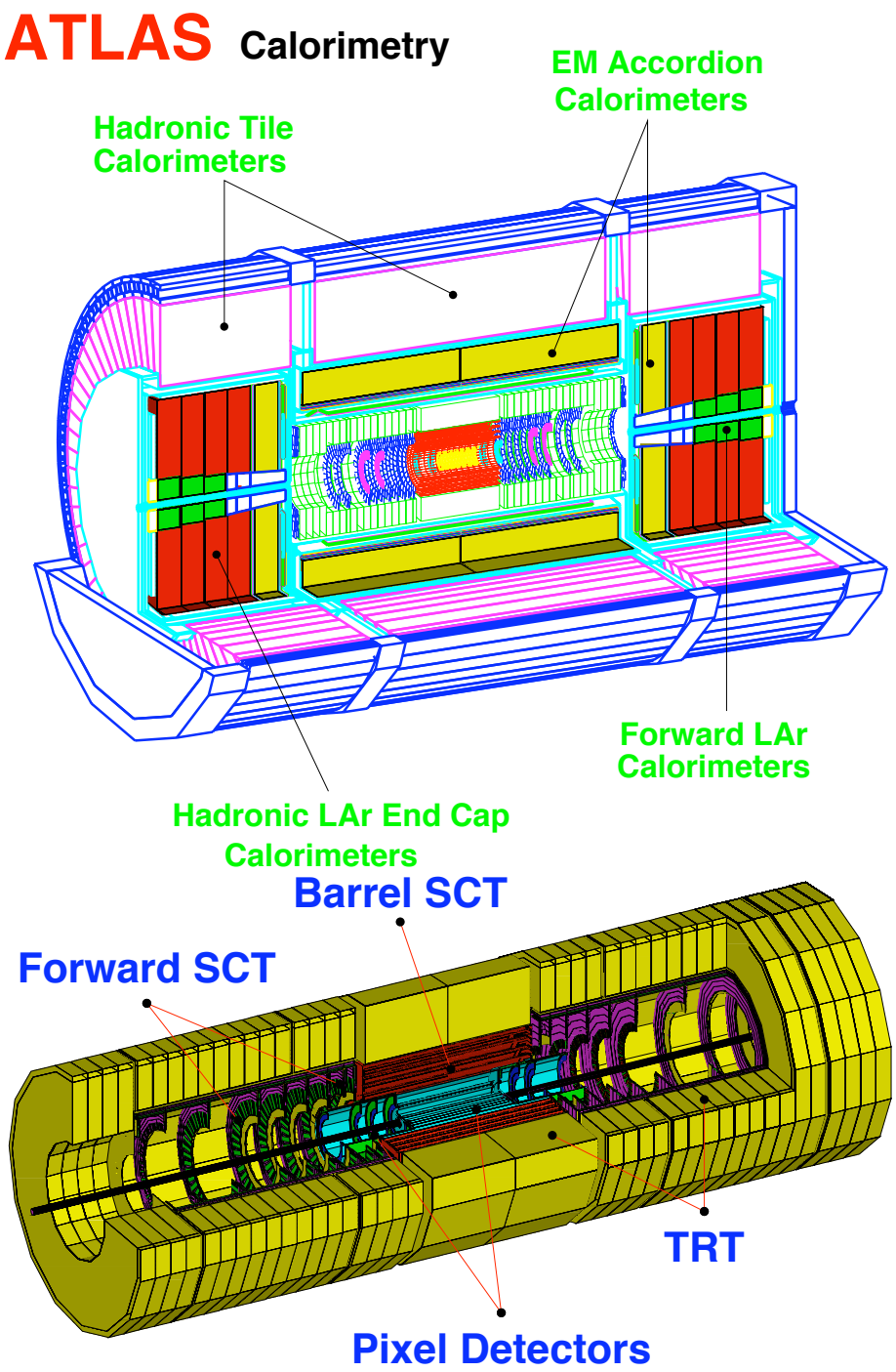

Figure 2.1: *View of the ATLAS detector. The huge muon system is not included. The inner detector is detailed below the overall description. Between the inner detector and the calorimeters, there is a super-conducting solenoid.*

- The outer tracker is a straw tube tracker, the TRT, which is described in detail in chapter 4. It gives a large number of tracking points and is reliable for pattern recognition. The occupancy includes complication due to pileups from adjacent bunchcrossing but expected to be reduced to $\sim$ 20 %.

The spatial resolution, $\sigma_{R\phi}$, is 10$-$15μm in the inner regions and $\sigma_{R\phi} is 170 \mu$m per straw in the TRT. The tracking precision in the TRT is $\sim 40\mu$m. In the direction along the beam and in the radial direction the resolution is worse, due to the uncertainty in the interaction point. However for the pixels, σ_z, $\sigma_R = 87\mu$m.

2.4 Trigger

The ATLAS trigger has to reduce the bunch crossing rate of 40.08 MHz to a maximum of 100 Hz to be able to record all events of highest interest. Considering the mean of 23 inelastic proton collisions per bunch crossing it has to be extremely efficient. Due to the large scope of physics studies it also has to be flexible. The trigger is organized in three levels, LVL1, LVL2 and LVL3.

1. At LVL1, special processors act on reduced granularity data from a subset of detectors. During processing the rest of the data is held in pipeline memories. The latency is about 2μs. The maximum output rate from the first level is 100kHz because it takes $\sim$ 10 μs to read out the data from the front-end systems. This corresponds to a reduction factor of 10^4.

2. The LVL2 trigger acts on the output from the LVL1. It uses data of full granularity and full precision from most of the detectors. The rate is reduced to about 1 kHz. The latency is $\sim$1-10 ms.

3. At LVL3, the full data is used to make the final selection of events to be recorded for off-line analysis. The decision time is 1 s. The rate is reduced to 10-100 MB/s by reducing the event rate or the event size.

The ATLAS trigger is programmable and will still be fine tuned while running experiences are achieved. The selection criteria are different for various physics channels. As an example, the B physics LVL1 trigger selects single muons with $p_T > 6$ GeV. At LVL2 a sharper p_T cut can be made. Additional requirements possible in LVL2 are to find final state particles of

the specific channel and cut on their p_T, for example a second muon, a high p_T electron or pairs of electrons or hadrons. At LVL3, full event information is used, including signatures such as displaced secondary vertices.

Chapter 3

The HERA-B Experiment

3.1 Introduction

The HERA-B experiment is primarily designed to detect CP violation in the asymmetry between the fraction of B^0 and $\bar{B}^0$ decaying to $J/\psi K^0_S$, where the J/ψ decays to a lepton pair. The rate of this signal is suppressed by a factor of 10^{-11} per inelastic event. Due to the smallness of the asymmetry and the total reconstruction efficiency of about 10%, 10 000 such golden events are needed per year.

The bunch crossing rate at HERA is 10 MHz, which is equal to about 10^{14} bunch crossings per year. Clearly more than one event per bunch crossing is needed for a CP measurement. The solution is to put target wires around the beam core in a manner described in fig 3.1. This configuration leads to four Poisson distributed interactions per bunch crossing.

The final state of the golden decay is a CP-eigenstate, which means that

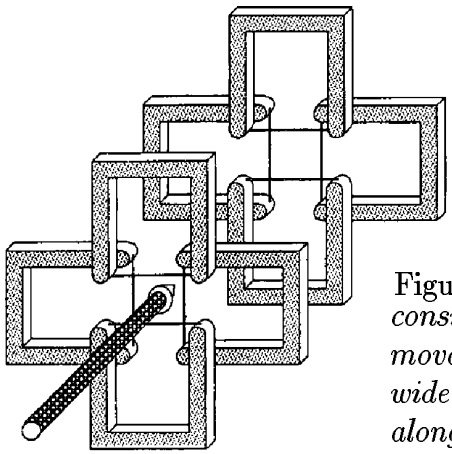

Figure 3.1: *Schematic view of the halo target, consisting of 8 metal ribbons on independently movable forks. The ribbons are about 50μm wide and 500μm thick. They are separated along the beam by about 5 cm.*

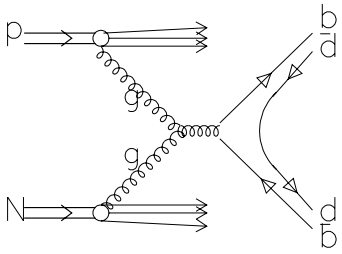

Figure 3.2: *A simplified example of the $b\bar{b}$ production mechanism in a hadron-nucleon collision. The fragmentation can lead to any other group of hadrons. In about 15% of the cases, the $b\bar{b}$ pair is instead produced by quark annihilation.*

it does not determine the flavor of the B meson. The b-quarks can only be produced in pairs (fig 3.2). The B meson under study is therefore always produced together with a B hadron of opposite flavor. This hadron is normally not decaying to a CP-eigenstate. The most common decay is to the lighter D-meson with the subsequent decay to a K-meson. Usually these decays are reconstructed and serve as a tag. Exclusive reconstruction has a high quality but poor efficiency. Other possibilities are to determine the charge of the Kaon or the lepton accompanying the D-meson. Another option is to geometrically reconstruct the decay vertex of the tagging B and count the charges of secondary tracks. Finally the charge of soft pions accompanying the B meson can serve as a tag. They come from either the decay of an exited B^{**} meson or from the local charge conservation in the quark fragmentation process. The combination of all these methods will bring the *tagging power* to the calculation of the precision of the CP measurement.

Since the b-quark quantum number is not conserved in weak interactions, the B^0 and $\bar{B}^0$ mix to the physical mass eigenstates, which are compounds of B^0 and $\bar{B}^0$. If there were no CP violation these compounds would be equal to the CP eigenstates. Due to the mass difference between the mass eigenstates, the asymmetry is oscillating with time. The decay time of the B meson has to be measured as the flight distance in the detector. This is the distance between the main vertex at a target wire and a displaced secondary decay vertex.

The experimental program also includes charm physics but especially B physics. Some examples are CP violation in other decay modes, studies on $B^0 - \bar{B}^0$, $B_s^0 - \bar{B}_s^0$ and $D^0 - \bar{D}^0$ mixing and properties of the Λ_b hadron.

3.2 Requirements

The goal to reconstruct the rare B decays in the environment of a very high track density demands a careful choice on trigger and detector design. In particular a fast readout is required due to the high bunch crossing rate.

The hardware has to be radiation hard. It will be exposed to $3 \cdot 10^7/\mathrm{R}^2$ particles per second, which corresponds to for example 100kRad/year at a distance R=10cm from the beam. For cost reasons and to pay regard to the other experiments around HERA (H1, ZEUS and Hermes), the components have to operate one year at full rate before they can be replaced.

The requirements on precise measurements in the full kinematic region and the profile of the signal put the special requirements on the HERA-B detector:

- Large geometrical acceptance.
- A fine granularity tracker.
- Reconstruction of multiple secondary vertices at ~ 1 cm from the beam. At this position the annual radiation dose is 10MRad.
- Efficient muon and electron identification. This is particularly important for the reconstruction of the J/ψ from the golden decay. A J/ψ candidate is selected already at the first triggering stage.
- Efficient kaon identification. This concerns the reconstruction of $\mathrm{K}^0_S \rightarrow \pi^+\pi^-$ from the decay of the neutral B in the golden channel, but more pronounced the separation of charged Kaons of the tagging B in the same event, from copious production of pions and protons.

All the mentioned requirements, except from the charged kaon identification, have their analogy in the ATLAS experiment.

3.3 Detector Design

The HERA-B detector (fig 3.3) is a large acceptance forward spectrometer covering 10 mrad up to 160 mrad vertically. This corresponds to 90% of the coverage in the center of mass system.

For momentum measurements, the tracks are bent horizontally in an inhomogeneous magnetic field of 2.2 Tm and of a radius of about 140 cm. The field is produced by a dipole magnet, centered at about 4.5 m from the target. In this bending plane the acceptance is increased up to 250 mrad.

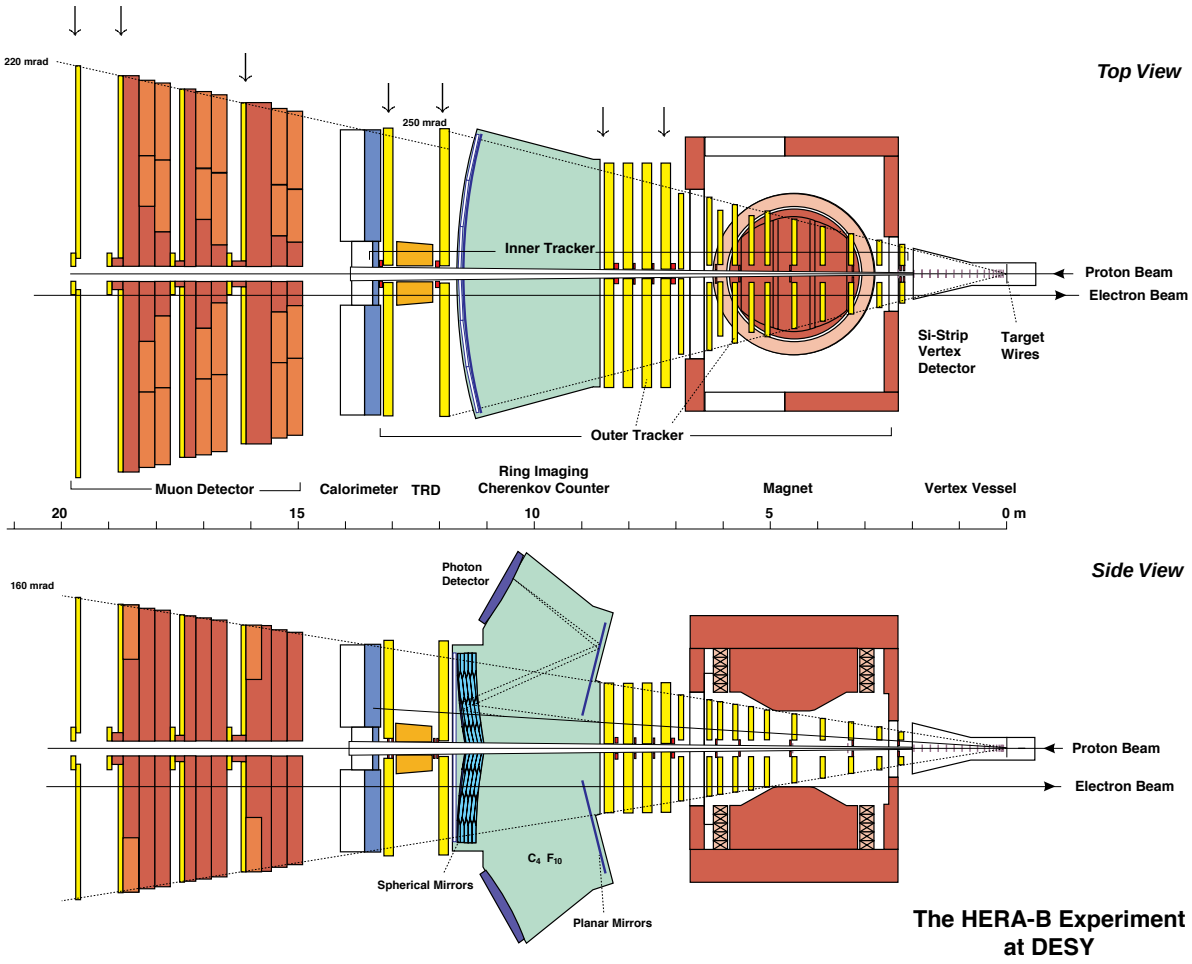

Figure 3.3: *The design from September 1996 of the HERA-B detector. Planes used in the First Level Trigger are pointed out by arrows above the upper figure.*

The precise reconstruction of multiple displaced vertices rely on several stereo layers of Silicon Strip Detectors, positioned close to the target. The target wires and vertex detectors are placed in a vacuum tank, named the Vertex Vessel in the figure.

Behind the magnet and the main part of the tracking system, there is a large Ring Imaging Čerenkov Counter (RICH). The task of the RICH is to separate charged kaons from pions and protons.

The requirements on lepton identification are carried out by the electromagnetic calorimeter, the TRD and the muon system, supplemented by track information.

The electromagnetic calorimeter (ECAL) is placed ~13 meters downstream. The middle and outer calorimeter modules are lead/scintillator sampling calorimeter read out by scintillating fibers in a way called the "shashlik" type. The energy resolution of the middle and outer parts is

$$\frac{\Delta E}{E} = 1\% \oplus \frac{9.5\%}{\sqrt{E}} \tag{3.1}$$

At the inner positions where the track density is very high, tungsten-alloy absorbers are used. The resolution of the inner modules is

$$\frac{\Delta E}{E} = 1.6\% \oplus \frac{17\%}{\sqrt{E}} \tag{3.2}$$

In addition to electron identification, the ECAL is also supposed to measure the energy of photons.

The purpose of the TRD is to separate electrons from hadrons. It is described in detail in chapter 4.

The penetrating muons are separated from hadrons using a hadron absorber. Three steel absorber blocks are alternated with muon chambers to link the muon hits with the tracks in the rest of the tracking system. The HERA-B detector system ends with a sole fourth muon superlayer, to provide a clean measurement of track direction after the filter.

Tracking System

The granularity of the tracking system varies with distance from the beam in order to limit the occupancy and minimize the number of channels. The overall occupancy with the chosen technologies has been found by Monte Carlo simulations to be $\sim 20\%$. In the pattern recognition regions it must be limited to $<15\%$. The tracking system is divided in three different technologies depending on the distance from the beam:

- 1cm - 6cm. Silicon strip of the same technology as the vertex detector. The spatial resolution is $\sigma_{xy} = 25\mu m,\ \sigma_z = 500\mu m$.

- 6cm - 20cm. Inner Tracker. In the initial plans the technical solution was focused on Micro-Strip Gaseous Chambers. Lately, the concentration is switched to optical fibers, which includes a system of scintillation fibers, light guide fibers and photomultipliers. The desired resolution is $\sim 80\mu m$.

- $>$ 19cm. Outer Tracker. Drift tubes in a honeycomb structure. The spatial resolution is $\sim 150 - 200\mu m$.

Silicon strip detectors are placed in the first half of the magnet, where the track density is very high.

The inner and outer tracker chambers in the magnet will be used for finding the curvature of tracks. The chambers in the field free region between the magnet and RICH are mainly used for pattern recognition of straight tracks. There are also inner and outer tracker chambers in front of the calorimeter, to extrapolate tracks to clusters in the calorimeter and to the muon system.

Inside and directly behind the magnet there are also three additional pad chambers. They are used for a High P_T hadron extension of the trigger. Its primary purpose is the search for $B^0 \to \pi^+\pi^-$ decays.

3.4 Trigger

Although the $b\bar{b}$ cross section has not been measured for HERA-B kinematics the order of magnitude is expected to be a few nb.

$$\frac{\sigma(pN \to b\bar{b} + X)}{\sigma_{inelastic}} \sim 10^{-6}. \tag{3.3}$$

At least one neutral B is formed in as much as 80 % of the cases. The branching ratios of the interesting B decay modes are very small.

$$\mathrm{BR}(B^0 \to J/\psi K_S^0) \cdot \mathrm{BR}(J/\psi \to \ell^+\ell^-) \cdot \mathrm{BR}(K_S^0 \to \pi^+\pi^-) = 4 \cdot 10^{-5}. \tag{3.4}$$

The signal of a golden event is accordingly suppressed by a factor 10^{-11}. At a bunch crossing rate of 10 MHz, the rate of interesting signals is much less than 1 Hz. The mean number of interactions per crossing is 4, leading to 120-200 tracks per event in the detector.

These conditions form the requirement on the trigger to be extremely fast and selective. In total the rate has to be reduced from 10 MHz to less than 100 Hz. The realization is based on a three level trigger system.

Concentration is put here on the, for the golden channel, most relevant J/ψ trigger.

1. In the first level the rate is reduced from 10 MHz to 50 kHz in 12μs. The data flow to filter is 150 GByte/s.

   A pretrigger will select high E_T clusters in ECAL or muons by a pattern after the muon absorber (or hadrons by very high p_T track in the high p_T chambers).

   The tracks of found lepton pair candidates are followed towards the target using techniques from Kalman filtering. The planes used in the first level trigger for the fast track reconstruction is indicated in fig. 3.3

   The tracks are constrained to origin from the target region and cuts are applied on the momenta, the p_T and the invariant mass, which is required to be around the J/ψ-mass.

2. In the second level, the rate is reduced further to 2 kHz. The average latency is about 1 ms. The input rate is 1.8 GByte/s.

   Tracks are propagated through the magnet and followed through SVD. In addition, the information of drift times is used and the χ^2 of the tracks are computed. The vertex quality for 2-track triggers is checked.

   If possible, a cut on vertex separation will be applied already at this stage. This is the main cut to reduce the immense background from direct production of J/ψ and other sources of high p_T leptons.

3. The processing time of the third level is 100 ms and the data flow is 140 MByte/s.

   The aim is B reconstruction. The track-fits and vertex-fits are refined and momentum cuts are reapplied. Particle identification will be done.

The output of the full event reconstruction is stored on tape for detailed analyses like B-flavour tagging and calculation of physical properties.

Chapter 4

Transition Radiation Detectors

4.1 Introduction

A charged particle moving in a medium emits radiation if either the velocity of the particle or the phase velocity of electromagnetic waves changes. If the medium changes, the radiation is due to a change in the phase velocity of the wave. This is *transition radiation* (TR). If it is the particle velocity that changes, the radiation is known as bremsstrahlung.

For ultrarelativistic particles, the transition radiation extends into the X-ray region. This makes the phenomenon useful in particle detectors. Because of its strong dependence on the Lorenz factor of the particle, $\gamma = E/mc^2$, it can provide particle identification at energies where other methods of detection become marginal (e.g Čerenkov radiation and time of flight methods).

In an interface between two different dielectric media, the number of photons radiated per particle is only of the order of the fine structure constant, α. Accordingly, the number of boundaries in a transition radiation detector has to be optimized. The minimum space required between the boundaries is proportional to the radiation wavelength. Also in this aspect the nature of the X-ray region is an advantage.

This chapter includes a theoretical overview of transition radiation based on the articles [4], [6] and [7] and a look into the Transition Radiation Tracker (TRT) in ATLAS. The HERA-B Transition Radiation Detector (TRD) is also presented.

4.2 Transition Radiation

In a theoretical description, the transition radiation is a solution to the homogeneous Maxwell equations. It is added to fulfill the boundary conditions

between two solutions of the inhomogeneous Maxwell equations when a particle passes.

In the superrelativistic limit, the radiation has a sharp maximum at small angles and high frequencies. At high frequencies, the medium can be considered as a gas, with electron density n_e and plasma frequency $\omega_p = \sqrt{4\pi\alpha n_e/m_e}$. The dielectric constant $\epsilon(\omega)$ of the medium is therefore given by

$$\epsilon(\omega) = 1 - \frac{\omega_p^2}{\omega^2} = 1 - \xi^2. \tag{4.1}$$

Bringing this substitution into the solution of the homogeneous Maxwell equation in the approximation of high γ and small angles, θ, the intensity of radiation emerging from a surface takes the form

$$\frac{\mathrm{d}^2W}{\mathrm{d}\omega\mathrm{d}\Omega} = \frac{\alpha}{\pi^2}\left|\frac{\theta}{\gamma^{-2}+\theta^2+\xi_g^2} - \frac{\theta}{\gamma^{-2}+\theta^2+\xi_f^2}\right|^2. \tag{4.2}$$

ξ_g and ξ_f are the deviations from unity of the dielectric constants of the two mediums.

Towards the X-ray region, ξ_i approach the order of γ^{-1}. In the ideal situation, when a particle crosses the boundary from medium to vacuum, the integrated intensity is proportional to γ. In practice however, this proportionality can not be preserved. The lower density medium is usually a gas instead of vacuum. A large influence comes also from the low energy cut-off, since the mean number of photons diverges in the soft X-ray region. The remaining number of photons per interface is only of the order of α. Consequently, many layers of boundaries are needed in order to detect transition radiation.

The Formation Zone

The total radiation from many boundaries (as in fig. 4.1), is a sum of the fields from the individual boundaries times factors accounting for interference and absorption. In the case of n parallel surfaces separating $n+1$ media, the total amplitude emerging from the last surface is proportional to

$$E(\omega,\vec{\theta}) = \sum_{j=1}^{n} \vec{e}^{j}(\omega,\vec{\theta})\exp\left(\sum_{m=j}^{n}\sigma_m + i\phi_m\right). \tag{4.3}$$

In this expression, backward emission and reflections have been neglected. This is justified due to the peak in the forward direction at high particle

energies. $\vec{e^j}$ is proportional to the single surface amplitude as in (4.2):

$$\vec{e^j} = \frac{\vec{\theta}}{\gamma^{-2} + \theta^2 + \xi_{j-1}^2} - \frac{\vec{\theta}}{\gamma^{-2} + \theta^2 + \xi_j^2}. \tag{4.4}$$

$\vec{\theta}$ is the difference between the directions of the photon and the particle.

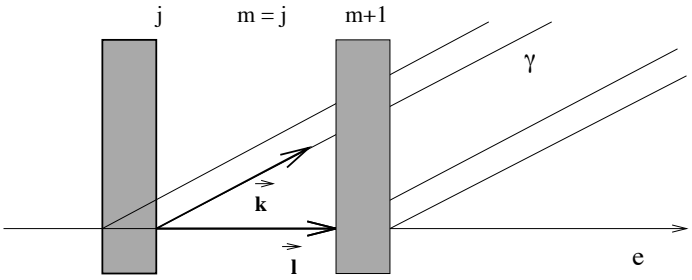

Figure 4.1: *The multi layer situation. The wave vector,* $\vec{\mathrm{k}}$*, and length vector,* $\vec{\mathrm{l}}$*, determine the phase difference between radiation from different boundaries.*

The effect from absorption in the mth medium is described by the factor e^{σ_m}. Due to the different speeds of the particle and the photon there is a phase difference between the two boundaries of the mth medium:

$$\phi_m = \frac{\omega l_m}{v} - \vec{k}_m \vec{l}_m, \tag{4.5}$$

where $\vec{k}_m$ is the wave vector of the photon radiated at the first boundary and $\vec{l}_m$ is the length of the medium layer. If ϕ_m is small, there is a negative interference between the two photons. Consequently, a minimal layer thickness is required. For small emission angles,

$$\vec{k}_m \vec{l}_m = k_m l_m \cos\theta \simeq k_m l_m \left(1 - \frac{1}{2}\theta^2\right). \tag{4.6}$$

The layer thickness should be of the order of the *formation length*

$$z_m = \frac{1}{\frac{\omega}{v} - k_m \left(1 - \frac{1}{2}\theta^2\right)}. \tag{4.7}$$

Using 4.1 and the relation

$$k_m = \sqrt{\epsilon_m}\omega \tag{4.8}$$

and approximating

$$\frac{1}{v} \simeq 1 + \frac{\gamma^{-2}}{2}, \tag{4.9}$$

the formation length can be simplified to

$$z_m = \frac{1}{(\gamma^{-2} + \theta^2 + \xi_m^2)\omega} \tag{4.10}$$

and accordingly

$$\phi_m = \frac{(\gamma^{-2} + \theta^2 + \xi_m^2)\omega l_m}{2} \tag{4.11}$$

The Yield

In the case of one foil placed in a gas there are two boundaries with e_1 = -e_2. Neglecting absorption and remembering that $\xi_0 = \xi_2$, (4.3) and (4.2) lead to the differential yield:

$$\left(\frac{d^2W}{d\omega d\Omega}\right)_{\text{single foil}} = \left(\frac{d^2W}{d\omega d\Omega}\right)_{\text{single surface}} \cdot 4\sin^2(\phi_1/2). \tag{4.12}$$

The first maximum due to constructive interference is at $\phi = \pi$. This should give the optimal length of the foil. After angular integration this maximum is found around the length

$$l_f = 2\pi\frac{\omega}{\omega'^2_{P_1}}, \tag{4.13}$$

where

$$\omega'^2_{P_1} = \omega^2_{P_1} - \omega^2_{P_2} \tag{4.14}$$

If the foil is placed in vacuum (P_2=0), $dW/d\omega$ increases logarithmically with γ. With a gas (P_2 >0) there is a saturation at $\gamma \geq \omega/\omega_{P_2}$.

A stack of foils is called a radiator. The energy from a radiator with N equal foils with regular spacing has sharp peaks at the resonance angles:

$$\phi_1 + \phi_2 = 2p\pi \tag{4.15}$$

(p integer). Using (4.11) the spacing between the peaks is $\Delta cos\theta \simeq \lambda/(l_1+l_2)$, which is very small and very difficult to measure experimentally. Therefore the interesting property is the angular integration, which is very similar to the single foil distribution scaled by the effective number of foils, N_{eff}. N_{eff} is the number of layers in case of no absorption corresponding to the same output. When N increases the absorption is also increasing and for $N > 1/\sigma_m$, this results in a saturation. There is thus an optimal number of layers in a radiator.

Detector Realization

Due to absorption, the resulting yield in a real detector is constant for particles exceeding a threshold γ factor. In summary, a transition radiation detector works in practice as a threshold detector for particle identification.

The emitted X-rays are absorbed in for example a gaseous detector placed behind each radiator. The atomic number of the gas has to be chosen such that the absorption length is small for the energy of the emitted transition radiation. The optimal thickness for the detector is approximately one absorption length of the average radiation energy. Due to the strong dependence of the radiation energy on the absorption length, there is thus a cutoff at high energy X-rays as well as low energy.

In a detector with length L, there are in summary four parameters to be optimized in addition to the choice of materials:

- l_f = the foil thickness.
- l_m = the thickness of the gap between foils.
- N = the number of foils in a radiator.
- l_g = the thickness of the detecting gas.

The optimized radiators and detectors are sandwiched within the detector length to collect a sufficient number of TR X-rays for particle identification.

4.3 The ATLAS TRT

The ATLAS TRT is part of the tracker. The anode wires are spaced with about 8 mm (inner module). Signals above 200 eV are accepted. The TRT has a good spatial resolution using drift time information.

The additional task of the TRT is to separate electrons from hadrons. Electrons of reactions under study have a relativistic gamma factor $\gamma > 40$. With a certain probability they will give rise to transition radiation, which will produce a signal above a high threshold (4-5 keV). Hadrons have a gamma factor below the limit for the production of detectable transition radiation.

Material and Parameter Choices

The sensitive part of the TRT is a straw filled with a gas. A wire made of gold and tungsten in the center of the straw collects the signal. Xenon

is choosen as chamber gas because for efficient X-ray absorption a gas with large Z is required. In ATLAS, the detector gas is composed of 70% Xe, 10% CO_2 and 20% CF_4. The straws containing the gas have a 2 mm radius. This is optimized for X-ray energies of $\sim$ 6 keV, since the transition radiation energies range from 4 keV. The choice puts an upper limit of about 15 keV on the detectable radiation energies.

The radiator materials should be less absorbent to optimize the number of interfaces before saturation. The plasma frequency of a low Z material or thinner foils is low, making the TR spectrum softer. This has to be taken into account. The foil should also be self-supporting and practical to cast into thin sheets. The choice made in the ATLAS end-cap TRT is polypropylene (CH_2), spaced in air.

The foil thickness is optimized using (4.13) for $\omega \sim 6$ keV and the plasma frequencies of the chosen materials. The optimal number of foils per radiator has been determined experimentally. The minimal spacing between the foils is obtained using (4.10) for X-rays above 4 keV and angles above 0.2 mrad. The exact values are determined by the fixed length of the detector and the maximal performance in the counting of clusters or the measurement of the total energy deposited in the gas. In ATLAS, the foil thickness is 15μm. There are 12 layers between each straw of gas and the spacing is around 320 μm. Due to the limited space in the barrel-TRT all available volume around the straws have to be filled with radiator. This is achieved by using a polyethylene/polypropylene fibre radiator since it is impossible to do it with foils.

Geometry Design

The ATLAS TRT is divided in a barrel part and two end-caps (fig. 4.3). In the end-caps the radiator and straws are interspaced in layers. This report will concentrate on the central barrel, where the straws are placed longitudinally and surrounded by radiator. The optimal arrangement of straws in such a solution would be equidistant spacing throughout the azimuthal coverage and then repeating layers of such rings in the radial extension as in fig. 4.2. For construction reasons it is convenient to divide the barrel azimuthally

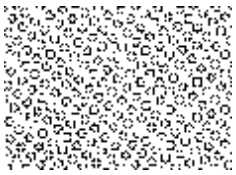

Figure 4.2: *The arrangement of straws in a homogeneous layer layout of a transition radiation detector. The radial direction goes from the lower left to the upper right corner.*

into sector-like modules, as described in fig. 4.4. With this geometry, the

uniformity is not preserved. The following study on the effect this has on the functioning of the TRT was made with a Monte Carlo simulation.

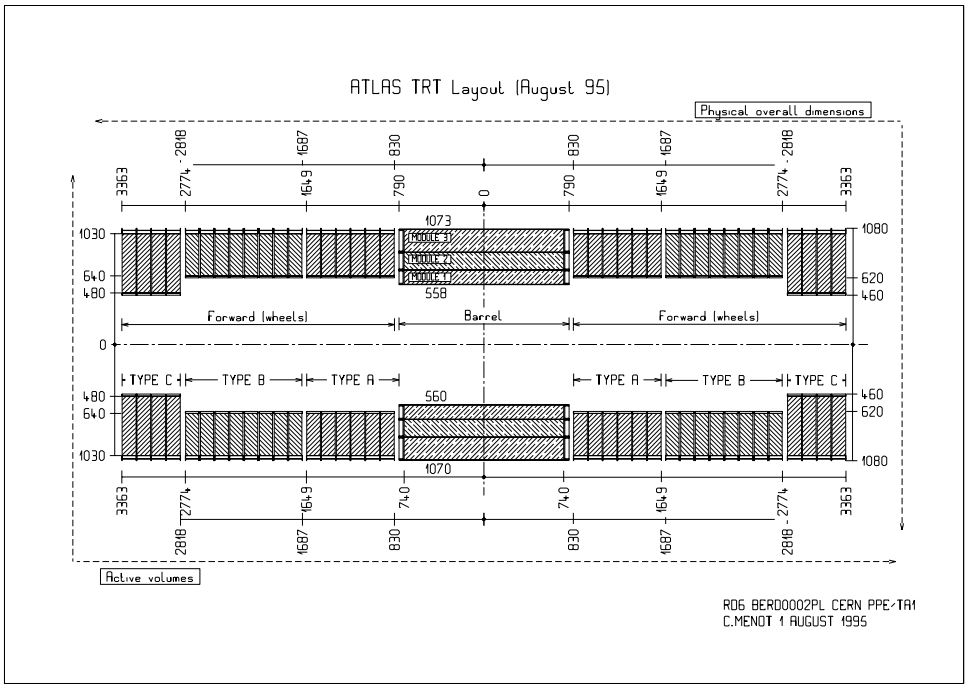

Figure 4.3: *The design of the Transition Radiation Tracker in ATLAS. The central part of the TRT (the barrel) is divided in three cylinders. Each cylinder consists of 32 modules. The straws are arranged longitudinally. In the end-cap TRT at high rapidities, the straws are placed radially in wheels.*

Particles of 40 GeV, produced by PYTHIA [24] have been sent at a rapidity of $\eta = \pm 0.3$ through a GEANT [28] simulation of the panel layout [8] of the inner detector using both the layer layout and the module layout of the barrel TRT. For the layer layout there is a peak at 36 number of straws, which are hit along the track. With the module layout there is a slightly broader distribution peaked at 34-35. The distributions are shown in fig 4.4a and fig 4.5a.

In the following a TR-hit is defined as a straw containing a high energy hit, i.e an energy deposition of more than 5 keV. The identification of a TR producing particle (an electron) is a minimum number of TR-hits as the particle traverses the barrel. The rejection power of the TRT is presented as the pion contamination divided by the electron identification efficiency:

$$R_{\pi/e} = \frac{\epsilon_\pi}{\epsilon_e} \tag{4.16}$$

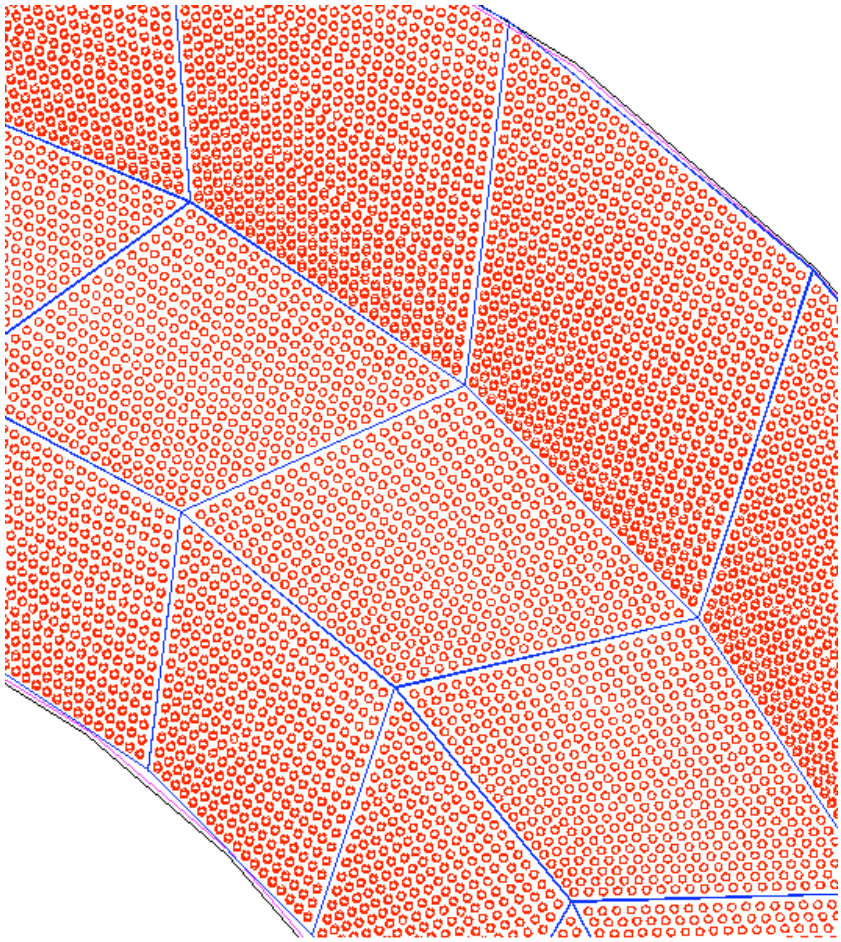

Figure 4.4: *The module layout of the barrel TRT described in [9] as drawn by GEANT[28]. A section of the barrel in the x-y plane is shown. The straws, walls and support contours are visible. There are three layers of modules, named depths. One module consists of rectangular layers of straws. Each depth consists of 32 modules. In the inner most depth there are 17 straw layers, in the second 21 and in the third, outer most depth there are 25 straw layers. The module walls are* 100 μm *thick. They are made of prepreg (*60% *carbon and* 40% *epoxy). The gaps between the module structure and the inner/outer supports are filled with* CO_2.

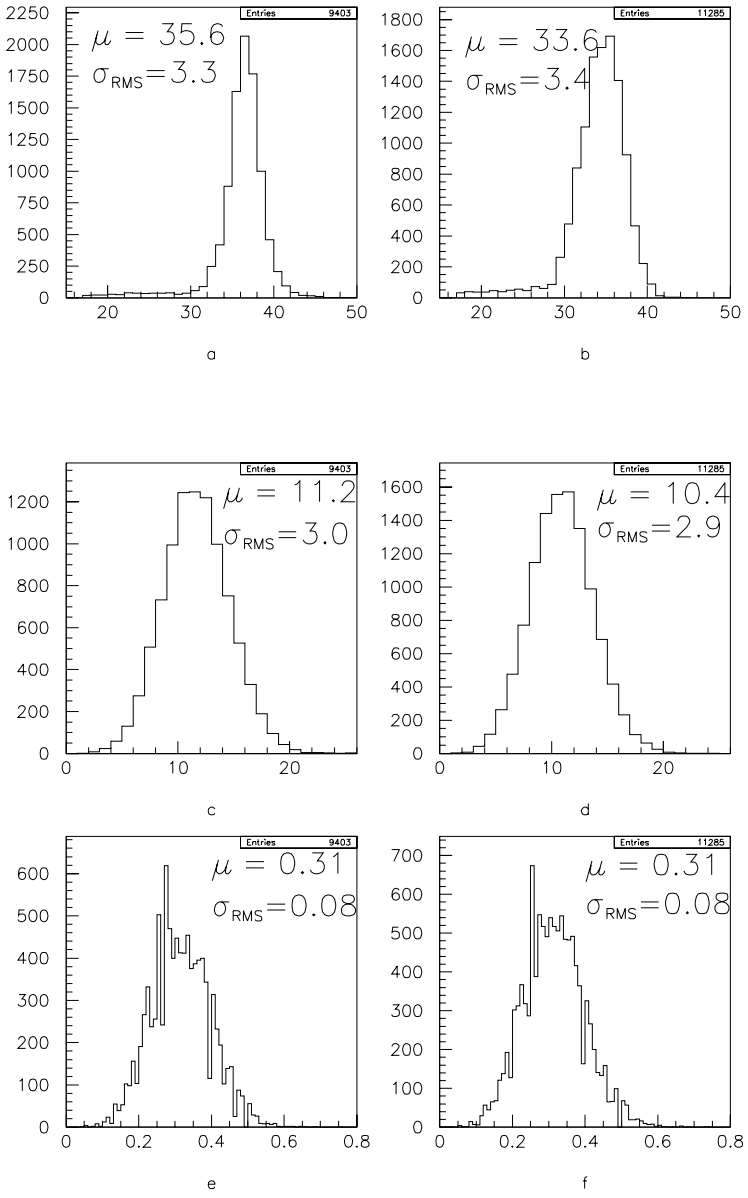

Figure 4.4: Single electrons sent through the layer (left) and the module (right) layout of the TRT. The number of straws hit in TRT (a,b), the number of straws with energy deposition of more than 5keV (c,d) and the ratio of such straws to the total number of straws hit (e,f).

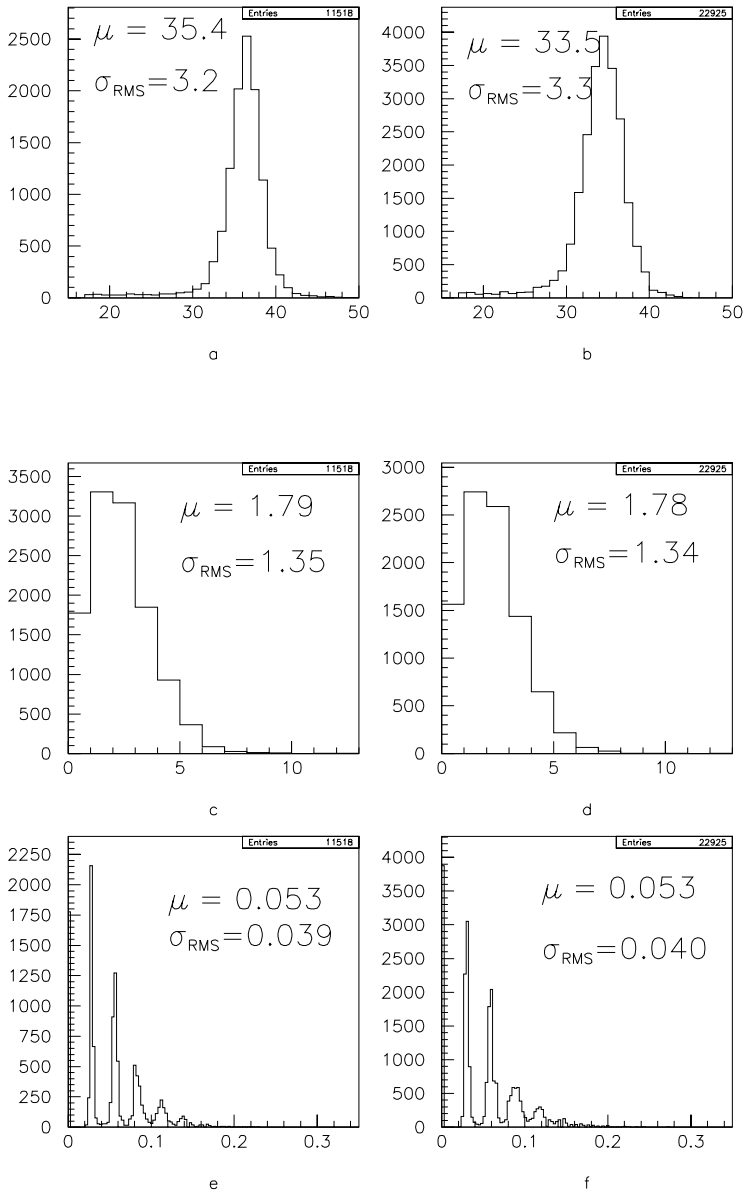

Figure 4.5: Single pions sent through the layer (left) and the module (right) layout of the TRT. The number of straws hit in TRT (a,b), the number of straws with energy deposition of more than 5keV (c,d), the ratio of such straws to the total number of straws hit (e,f).

and is normally quoted at a given electron identification efficiency of 90%.

The relative number of TR-hits is not strictly determined and the number of traversed straws depends on the depth of the detector. Therefore it may be informative to apply a hypothetical cut of fractions of TR-hits, which gives exactly 90% electron efficiency. With a homogeneous geometry this cut would be placed at 7.4 $\pm$ 0.1 TR-hits and lead to a pion contamination of roughly (0.24 $\pm$ 0.04)%.

Using the modular geometry the cut would be placed at 6.9 $\pm$ 0.1 TR-hits, leading to a pion contamination of about (0.35 $\pm$ 0.03)%, which is an increase of (62 $\pm$ 21)%.

The numbers are obtained by fitting the histograms in fig 4.4b and fig 4.5b.

Barrel TRT	*Layer Layout*		*Module Layout*	
40 GeV	*electrons*	*pions*	*electrons*	*pions*
Number of straws hit with energy deposition $>$ 200 eV	35.6 $\pm$ 3.3	35.4 $\pm$ 3.2	33.6 $\pm$ 3.5	33.5 $\pm$ 3.3
Number of TR-hits	11.2 $\pm$ 3.0	1.87 $\pm$ 1.38	10.4 $\pm$ 2.8	1.78 $\pm$ 1.34
In percentage of total	31.43 $\pm$ 0.08	5.31 $\pm$ 4.06	31.18 $\pm$ 0.08	5.32 $\pm$ 3.96
Detection efficiency, ϵ with cut on $>$ 6 TR-hits (%)	94.7 ($\pm$ 0.1)	0.40 ($\pm$ 0.02)	91.9 ($\pm$ 0.2)	0.35 ($\pm$ 0.03)
Rejection power R = ϵ_h/ϵ_l	0.0043 ($\pm$ 0.0003)		0.0039 ($\pm$ 0.0008)	

Table 4.1: The mean values and the RMS of the distributions for the old layer layout and the module layout of the barrel TRT in ATLAS. A TR-hit is a straw with more than 5 keV. The standard deviations on ϵ and R are calculated on sets of 2000 events. There is no significant difference between layer and module layout in the number of straws collecting a signal above the high threshold. A requirement of *at least* 90% electron detection efficiency, corresponds to a cut at more than 6 TR-hits and 95% (92%) electron detection efficiency, for the layer (module) layout. The number of pions which pass this cut is 0.40% and 0.35% respectively. No decrease in the rejection power, R $\sim$0.004, is observed for this size of the barrel.

In the realistic case, quoting the result in table 4.1, it is seen that a module geometry not significantly decreases the performance of the Barrel TRD.

4.4 The HERA-B TRD

The HERA-B TRD is based on proven technology from the ATLAS TRT developments (RD-6). It uses a similar fibre radiator (polypropylene) and gas (Xe/ CF_4/ CO_2). A track hits in mean 36 layers of straws interspaced with 15mm fibre radiator. The straw diameter is 5 mm.

The TRD modules are placed between the two tracker superlayers in front of the calorimeter in the central region, where the track density is very high and the hadron rejection power of the calorimeter is lower.

Hadron rejection of a factor 15 at 98% electron identification efficiency is planned for. Fast and high precision tracking make the TRD useful in the trigger. It could possibly be used already at the pretrigger level.

Chapter 5

B Physics and CP Violation

5.1 Introduction

The HERA-B experiment will give access to the system of B hadrons. Due to the large mass of the b-quark this family has a rich scope of decays to be studied. For heavy quarks ($m_Q \to \infty$) there is a symmetry, analogous to the chiral symmetry for light quarks. A range of measurements to be performed in the B system will be viewed from the Heavy Quark Effective Theory based on this symmetry. It is basically a summary of the articles [12] and [13].

Maybe more importantly, CP violation can be studied in a variety of ways in the B system. The detection and measurement of CP violation in the B system is the main goal of the HERA-B experiment.

The introduction to CP violation, particularly in the B system and in the golden channel is based on [13] and [14].

5.2 Heavy Quark Symmetry

The heavy quark symmetry relies on the division of QCD into perturbative and non-perturbative regions.

The effective coupling constant becomes weak in processes with large momentum transfer, which corresponds to interactions at short distances. This is known as asymptotic freedom. Interactions are described perturbatively.

Because of confinement of quarks and gluons, phenomena are described perturbatively on the length scale $R_{had} \sim 1/\Lambda_{QCD}$.

For a heavy quark, $m_Q \gg \Lambda_{QCD}$ and the effective coupling constant $\alpha_s(m_Q)$ is small. At length scales comparable to the Compton wavelength of the heavy quark, the strong interactions are described perturbatively.

The typical momenta exchanged between heavy and light constituents in a hadron are of the order Λ_{QCD}. Distances which can be resolved are of order R_{had}. However, the Compton wavelength of the heavy quark is much smaller than that, which means that quantum numbers like flavour and spin of the heavy quark can not be resolved. Only the colour field extends over large distances because of confinement.

Relativistic effects vanish as $m_Q \to \infty$. Such effects are colour magnetism and spin. The quark is at rest relative to the hadron as $m_Q \to \infty$. The effective result is that the heavy quark acts as a static color. This gives relations of heavy mesons like B, D, B^*, D^* or heavy baryons like Λ_b and Λ_c. The description of these hadrons only differ due to non-perturbative corrections in powers of $1/m_Q$ and perturbative corrections in powers of $\alpha_s(m_Q)$. For N_h heavy quark flavours, there is an SU($2N_h$) spin-flavour symmetry group, under which the effective strong interactions are invariant. The aim is to rewrite the Lagrangian for a heavy quark,

$$\mathcal{L}_Q = \bar{Q}(i\not{D} - m_Q)Q, \tag{5.1}$$

into an expansion of $1/m_Q$ in order to construct a low-energy effective theory, which is called the Heavy Quark Effective Theory (HQET).

A heavy quark has more or less the velocity of the hadron, v, and the momentum can be rewritten as

$$P_Q^\mu = m_Q v^\mu + k^\mu, \tag{5.2}$$

where the residual momentum k is small and is affected by interaction with light degrees of freedom like soft gluons. The quark field can be written as a sum of the large and small component fields h_v and H_v:

$$h_v(x) = e^{im_Q vx} P_+ Q(x), \quad H_v(x) = e^{im_Q vx} P_- Q(x), \tag{5.3}$$

where P_+ and P_- are projection operators

$$P_\pm = \frac{1 \pm \not{v}}{2}. \tag{5.4}$$

h_v annihilates a heavy quark with velocity v. It describes the massless degrees of freedom. H_v creates a heavy antiquark. It corresponds to fluctuations with twice the heavy-quark mass, which are the heavy degrees of freedom appearing as corrections to the effective Lagrangian. The derivation of the Lagrangian is well described in [12].

$$\mathcal{L}_{\text{eff}} = \bar{h}_v iv \cdot D h_v + \frac{1}{2m_Q}\bar{h}_v (iD_\perp)^2 h_v + \frac{g_s}{4m_Q}\bar{h}_v \sigma_{\mu\nu} G^{\mu\nu} h_v + O(1/m_Q^2), \tag{5.5}$$

where $[iD^\mu, iD^\nu] = ig_s G^{\mu\nu}$ is the gluon field-strength tensor. In the limit $m_Q \to \infty$, only the first term remains. The second term arise from off-shell residual motion of the heavy quark. The third term describe the colour-magnetic coupling of the heavy-quark spin to the gluon field. Both these terms scale like $1/m_Q$.

One way to test HQET is in spectroscopy. The mass of the hadron should be the mass of the heavy quark plus a term which is independent of the flavour (up to corrections).

Exclusive semileptonic decays of B mesons are studied to extract values of $|V_{cb}|$ and $|V_{ub}|$ in the CKM matrix (5.11). The description of semileptonic decays includes form factors. The Heavy Quark Symmetry implies relations between form factors of different heavy mesons, because in the limit $m_Q \to \infty$, the form factor can only depend on the Lorenz boost $\gamma = v \cdot v'$. Matrix elements of scattering of heavy quarks or decays to other heavy quarks are all determined by the Isgur-Wise function $\xi(v \cdot v')$, $\xi(1) = 1$. For example for the decay of a $\bar{B}$ meson into a D meson:

$$\frac{1}{\sqrt{m_B m_D}} \left\langle D(v')|\bar{c}_{v'}\gamma^\mu b_v|\bar{B}(v)\right\rangle = \xi(v \cdot v')(v + v')^\mu. \tag{5.6}$$

Additional spin rotation factors appear in the relation between vector mesons and pseudoscalar mesons.

Non-perturbative power corrections $(\Lambda_{QCD}/m_Q)^n$ are added as before, however more complicated in the case of weak-decay form factors. Perturbative corrections of order $\alpha_s^n(m_Q)$ are also applied to account for short distance interactions, which do resolve the spin and flavour of the heavy quark. The combined result is that $\xi(v \cdot v')$ is replaced by

$$\mathcal{F}(v \cdot v') = \mathcal{F}(1)[1 - \hat{\varrho}^2(v \cdot v' - 1) + ...]. \tag{5.7}$$

$\mathcal{F}(1)$ is calculated with HQET including power corrections. The slope can be measured experimentally and extrapolations to zero recoil can be made. In such a way $|V_{cb}|$ can be extracted from the semileptonic decay

$$\frac{\mathrm{d}\Gamma(\bar{B} \to D^*\ell\bar{\nu})}{\mathrm{d}(v \cdot v')} = k\,|V_{cb}|^2\mathcal{F}^2(v \cdot v'), \tag{5.8}$$

where k is a kinematical constant.

The determination of $|V_{ub}|$ depends on form factors for heavy to light meson transitions, where the heavy quark symmetry does not help.

$|V_{cb}|$ can also be determined from inclusive B decays. HQET applies to the theoretical expressions of the decay widths like before with the perturbative corrections in powers of $\alpha_s(m_B)$.

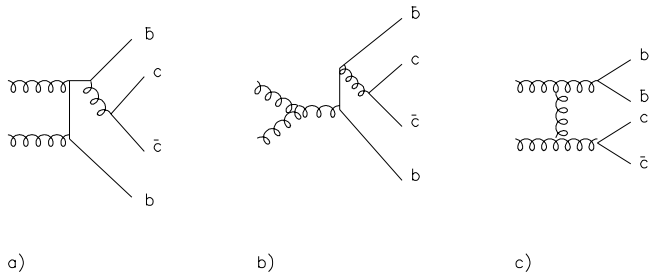

Figure 5.1: Some typical Feynmann diagrams for the subprocess g + g $\rightarrow B_c^+$ + b + $\bar{c}$. The fragmentation type diagrams, a) and b), have $c\bar{c}$-pairs created on the leg of a $\bar{b}$. In the recombination type diagram c), the quark- antiquark pairs are created independently.

The semileptonic branching ratio and the average number of charm hadrons per B decay (known as charm counting) are other challenges for HQET as well as lifetime predictions.

5.3 B_c Mesons

Among the heavy quark states, the ($\bar{b}c$) system takes a particular place. Since top quarks are too heavy to form a stable state, ($\bar{b}c$) is the only system, composed of two heavy quarks, which can not decay strongly nor electromagnetically. The study of B_c mesons can increase the understanding of QCD dynamics and important parameters of the electroweak theory.

The question has been raised whether HERA-B holds the possibility to observe B_c mesons. The predictions on the total cross section of B_c production at HERA-B do not give precise information except that it is small. It is suppressed by a hard production of the additional c-quark and a small probability of the ($\bar{b}c$) state formation. At HERA-B there is a strong threshold effect because additional pairs of heavy B and D mesons have to be produced [10]. The two first diagrams in fig. 5.1 describe $b\bar{b}$ production and subsequent fragmentation of a $\bar{b}$-quark. The fragmentation of a c-jet contributes too, but it is less important than that of a b-jet. The contribution of recombination diagrams is not negligible at p_T values below 10 GeV. According to [10],

$$\sigma_{B_c} = 0.07 - 0.08 pb.$$

on the other hand [11] present

$$\sigma_{B_c} = 0.002 - 0.09 pb.$$

The interaction frequency could be as much as 50-60 MHz. In a nominal year of 10^7 seconds about 100-2300 B_c mesons would then be produced in HERA-B.

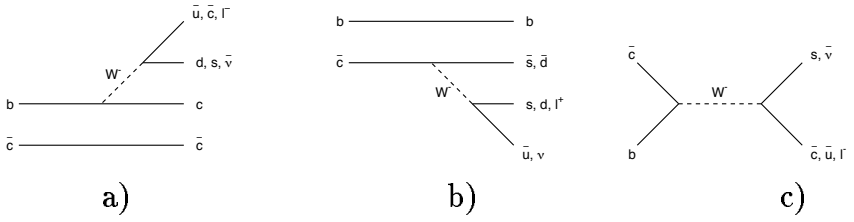

a) b) c)

Figure 5.2: *The decay of B_c mesons. a) and b) are the semileptonic and nonleptonic spectator decays and c) illustrates nonleptonic weak annihilation.*

The B_c mesons can decay via three main processes as is shown in fig. 5.2, leading to a numerous amount of different decay products. The HERA-B trigger is a dedicated J/ψ trigger. Therefore it is advantageous to search for B_c in decays to J/ψ. The inclusive decay rate to J/ψ is 20%. The decay mode $B_c \rightarrow J/\psi\pi$ deserves special attention. All of the three final state particles can be well reconstructed and allow for a mass reconstruction of the B_c meson. They also have a common secondary vertex, which makes the topology very clean. The invariant mass of the lepton pair from the J/ψ supplies an additional constraint on the secondary vertex. The branching ratio of this channel is equal to

$$BR(B_c^+ \rightarrow J/\psi\pi^+) \approx 0.2\ \%\ [10].$$

Including the branching ratio of J/$\psi \rightarrow l^+l^-$, it follows that only at maximum one B_c signal event can be expected every second year in HERA-B. This is of course not possible to detect in the background of all other B decays.

There are many other channels, which could add up the statistics. The decay mode $B_c \rightarrow J/\psi\ell\nu$ has an expected branching ratio of $\approx 3\%$ leading to at a maximum 7 events per year. This is obviously also too low for an observation.

5.4 CP Violation

Introduction

CP is the combined effect of charge conjugation and parity transformation. Charge conjugation flips the signs of internal charges, such as the electric charge, the baryon number and lepton numbers. Under parity operation the

space coordinates are reversed so that for example the direction of motion is reversed. The spin is not affected.

Whereas P and C are not conserved in weak interactions, the combined operation CP was long thought to be a good symmetry in all types of interactions. Violation of CP symmetry was first discovered in the long-lived neutral K meson. All field theories are automatically invariant under the succession of C, P and T (time reversal) operations due to the requirement that the Lagrangian be hermitian and invariant under Lorenz transformations. Some consequences of this *CPT* theorem is that particles and antiparticles have the same masses and lifetimes.

The consequence of CP violation or equally T violation is in very generalized words the sense of a direction of time in the evolution of history. It is believed that, in the early stages of our universe, CP violation resulted in an excess of matter over antimatter, which lead to the observed baryogenesis.

The Standard Model (SM) prediction is too small to account for the observed baryon asymmetry in the universe. Therefore, measurements of CP violation are of high interest. Due to its smallness, CP violation is one of the least tested properties of the Standard Model. Exploration of the B system gives access to new sources of CP violation, which will lead to more precise measurements of the CP-violating parameter in the Standard Model. It might also indicate scenarios for CP violation beyond the Standard Model.

Theoretical Description

Theories within the Standard Model include CP violation in both strong interactions (QCD) and electroweak interactions. If there is CP violation in strong interactions it has been shown experimentally to be very small (e.g [14] and [15]).

In the Electroweak Model the CP violation is incorporated in the CKM (Cabbibo, Kobayashi, Maskawa) matrix which describes the weak interaction between the quarks, i.e. the flavour-changing charged current interactions:

$$\mathcal{L}_{int} = -\frac{g}{\sqrt{2}}(\bar{u}'_L, \bar{c}'_L, \bar{t}'_L)\gamma^\mu \begin{pmatrix} d'_L \\ s'_L \\ b'_L \end{pmatrix} W^+_\mu + h.c. \tag{5.9}$$

Here q'_L are the left-handed quark doublets. Due to interaction with the Higgs doublet, these are nonphysical fields, having a non-diagonal mass matrix. The CKM matrix appears when the Lagrangian is written in terms of the mass eigenstates:

$$\mathcal{L}_{int} = -\frac{g}{\sqrt{2}}(\bar{u}_L, \bar{c}_L, \bar{t}_L)\gamma^\mu V_{CKM} \begin{pmatrix} d_L \\ s_L \\ b_L \end{pmatrix} W_\mu^+ + h.c. \,, \tag{5.10}$$

where

$$V_{CKM} = \begin{pmatrix} V_{ud} & V_{us} & V_{ub} \\ V_{cd} & V_{cs} & V_{cb} \\ V_{td} & V_{ts} & V_{tb} \end{pmatrix} \tag{5.11}$$

is the unitary CKM matrix. It has 9 parameters (the square of the dimension). There are 3 Euler angles in three dimensions. Those are the quark mixing angles. The rest of the parameters are phases.

The phases of all the quark fields are arbitrary, not measurable quantities. Under phase transformation of the quark fields, V_{jk} is replaced by $e^{i(\phi(k)-\phi(j))}V_{jk}$. There are accordingly 5 unmeasurable phases and only one measurable phase. This phase is the origin of CP violation in the Standard Model.

The CKM matrix is often written in the Wolfenstein parameterization, which is an expansion in powers of $\lambda = |V_{us}| = cos\theta_C$, where θ_C is the Cabbibo angle known from the mixing of two generations.

$$V_{CKM} \simeq \begin{pmatrix} 1-\frac{\lambda^2}{2} & \lambda & A\lambda^3(\rho - i\eta) \\ -\lambda & 1-\frac{\lambda^2}{2} & A\lambda^2 \\ A\lambda^3(1-\rho-i\eta) & -A\lambda^2 & 1 \end{pmatrix} + O(\lambda^4). \tag{5.12}$$

A, ρ and η are real numbers of order unity as indicated by experiments. $|V_{ud}|$ and $|V_{us}|$ are known to better than 1% accuracy. $|V_{cd}|$ and $|V_{cs}|$ are known to 10-20%. $|V_{cb}|$ is known to 5% accuracy. Hence both λ and A are well determined experimentally.

$$\lambda = 0.2205 \pm 0.0018, \; A = \left|\frac{V_{cb}}{V_{us}^2}\right| = 0.8 \pm 0.04. \tag{5.13}$$

$|V_{ub}|$ and $|V_{td}|$ are known to 30%, implying a high uncertainty in ρ and η. $|V_{td}|$ is obtained from $B^0 - \bar{B}^0$ mixing and $|V_{ub}|$ from charmless decays of B mesons. The phase is accessible as described below.

The unitary condition of the CKM matrix yields the following relations:

$$V_{ij}V_{ik}^* = 0 \;\; (j \neq k). \tag{5.14}$$

Among those, the relation

$$V_{ud}V_{ub}^* + V_{cd}V_{cb}^* + V_{td}V_{tb}^* = 0 \,, \tag{5.15}$$

deserves special attention, since the phases between V_{ub}, V_{cd} and V_{td} are large and can be detected in beauty decays. The condition can be presented as a triangle. Below, the sides are rescaled by $V_{cd}V_{cb}^*$ and $\bar{\rho} = \left(1 - \frac{\lambda^2}{2}\right)\rho$, $\bar{\eta} = \left(1 - \frac{\lambda^2}{2}\right)\eta$.

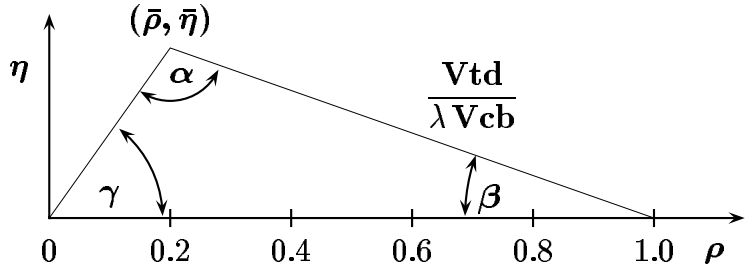

If CP would be conserved, the quark mixing matrix would be real and the triangle collapse to a line. Detected CP violation in the $K^0 - \bar{K}^0$ mixing has constrained the triangle to non-zero values of the η parameter. In particular, combined with calculations on the rate of $B^0 - \bar{B}^0$ mixing,

$$0.34 < \sin 2\beta < 0.75. \tag{5.16}$$

Experimental Observation

The only unambiguous measurement of CP violation is in the decay of K_L. As explained above, the effect of CP violation is expected to be larger in the B system. The methods to extract the value of the CP violating parameter in the electroweak model from decays of B mesons will be discussed in the remaining part of this chapter.

Three manifestations of CP violation in pseudoscalar mesons can be distinguished: Direct CP violation, indirect CP violation and the interference between the two.

Direct CP violation results from interference of decay amplitudes in the weak decays. CP is the combined effect of charge conjugation and parity transformation. For pseudoscalar mesons, this means:

$$CP|P(\vec{p})\rangle = e^{i\varphi_P}|\bar{P}(-\vec{p})\rangle\,. \tag{5.17}$$

P and $\bar{P}$ are CP conjugated states. The phase is unmeasurable and arbitrary.

Consider the decays of CP conjugated pseudoscalar meson states (e.g B^+ and B^- or the neutral B mesons) to CP conjugated final states f and $\bar{f}$. The CP conjugated amplitudes are:

$$A = \langle f|\mathcal{H}|P\rangle = \sum_k A_k e^{i\delta_k} e^{i\phi_k},$$

$$\bar{A} = \left\langle \bar{f}|\mathcal{H}|\bar{P}\right\rangle = e^{i(\varphi_P - \varphi_f)} \sum_k A_k e^{i\delta_k} e^{-i\phi_k}. \tag{5.18}$$

The sum goes over all possible decay diagrams. δ_i appear in scatterings due to strong interactions. ϕ_i are the weak phases that violate CP.

The physically meaningful quantity is the absolute value of the ratio between the amplitudes.

$$\left| \frac{\bar{A}}{A} \right| \neq 1 \quad \Rightarrow \quad \text{Direct CP violation.} \tag{5.19}$$

If there is only one partial decay amplitude, the phase is unmeasurable. Interference between at least two diagrams is required. The candidates are found among those non-leptonic decays which receive contributions from both tree and penguin diagrams[1], or penguin diagrams only.

The hadronic uncertainties in direct CP violation are large because of poorly known hadronic matrix elements and strong phase shifts. Direct CP violation has not yet been measured experimentally.

Indirect CP violation arises in the mixing of neutral mesons. Due to mixing, P^0 and $\bar{P}^0$ form the mass eigenstates:

$$\begin{aligned} |P_1^0\rangle &= p|P^0\rangle - q|\bar{P}^0\rangle\,, \\ |P_2^0\rangle &= p|P^0\rangle + q|\bar{P}^0\rangle\,; \quad |p^2| + |q^2| = 1 \end{aligned} \tag{5.20}$$

If $p = q = 1/\sqrt{2}$ then

$$CP|P_1^0\rangle = |P_1^0\rangle\,, \quad CP|P_2^0\rangle = |P_2^0\rangle\,, \tag{5.21}$$

which is equal to the CP eigenstates. The physically meaningful probe is

$$\left| \frac{q}{p} \right| \neq 1 \quad \Rightarrow \quad \text{Indirect CP violation.} \tag{5.22}$$

Flavour eigenstates different from the CP eigenstates have been detected in the neutral K mesons. There exists yet another method to detect CP violation. The value of q/p is to the first approximation only a phase (as described in appendix A). Moreover, the calculation of $|q/p|$ involves poorly known hadronic matrix elements.

CP violation in the interference between mixing and decay gives access to the phases of the quantities $\bar{A}/A$ and q/p.

[1]Examples of each kind are given in the section about the golden decay.

In the decay of neutral mesons into CP eigenstates,

$$A = \left\langle f_{CP}|\mathcal{H}|P^0\right\rangle, \quad \bar{A} = \left\langle f_{CP}|\mathcal{H}|\bar{P}^0\right\rangle \tag{5.23}$$

the product

$$\lambda = \frac{q}{p} \cdot \frac{\bar{A}}{A} \tag{5.24}$$

is physically meaningful. This is because all phase convention dependence of q/p cancels against $\bar{A}/A$.

$$\lambda \neq 1 \quad \Rightarrow \quad \text{CP violation.} \tag{5.25}$$

In this case, interference between partial decays is not necessary and hadronic uncertainties can therefore be minimized. For many B decays it is true that $\bar{A}/A = \mathrm{e}^{2i\phi}$ as well as $q/p = \mathrm{e}^{-2i\beta}$ to first approximation. This gives

$$|\lambda| = 1, \text{ but } \ \mathrm{Im}\ \lambda = -\sin(2\beta - 2\phi). \tag{5.26}$$

The actual measurement in an experiment is the time dependent asymmetry between B^0 and $\bar{B}^0$ decaying to the same CP eigenstate:

$$a_{f_{CP}} = \frac{\Gamma(B^0(t) \to f_{CP}) - \Gamma(\bar{B}^0(t) \to f_{CP})}{\Gamma(B^0(t) \to f_{CP}) + \Gamma(\bar{B}^0(t) \to f_{CP})} \tag{5.27}$$

In the approximation $|\lambda| = 1$,

$$a_{f_{CP}} = -\mathrm{Im}\ \lambda \sin(\Delta x t), \quad x = \frac{\Delta m_B}{\Gamma}\ , \tag{5.28}$$

where Δm_B is the mass difference between the mass eigenstates of the B mesons, Γ is the inverse lifetime and t is measured in units of the lifetime. The proof for this is conveyed to appendix A.

The Golden Decay

The decay B $\to J/\psi K_S^0$ offers a very clean measurement of CP violation for four main reasons:

1. CP violation is expected to be large in $\mathrm{B^0}$-$\mathrm{\bar{B}^0}$ mixing.
2. The final state is a CP eigenstate.
3. The contamination from penguin diagrams is small.

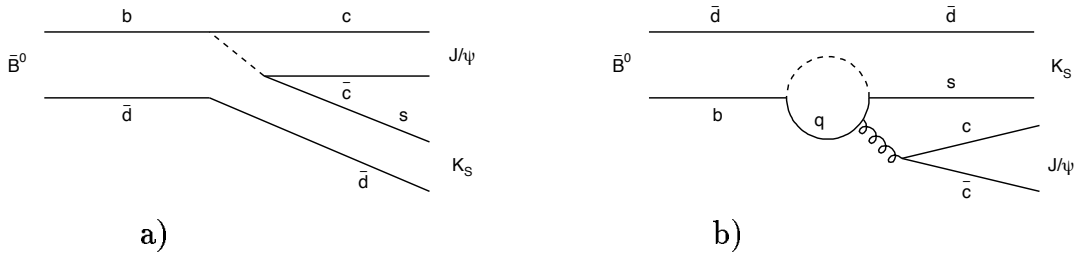

Figure 5.3: *The golden decay. a) The tree diagram and b) the penguin diagrams. The quark in the loop can be either t, c or u.*

4. It has a clear signature to pick out from a high combinatorial background.

The last point is explained in chapter 7. Because of these favourable conditions, the channel is labelled the *gold-plated* mode for measuring $\sin(2\beta)$.

The decay diagrams are depicted in fig. 5.3. The amplitude of the tree diagram is proportional to $\bar{A}_{tree} = V_{cb}V_{cs}^* = A\lambda^2 + O(\lambda^4)$.

There are three types of penguin contributions. Each with a t, c or a u-quark in the loop. All penguin diagrams are suppressed due to this loop. The amplitude of the t-quark diagram is proportional to $V_{tb}V_{ts}^* = -\bar{A}_{tree} + O(\lambda^4)$. With a c-quark the amplitude is proportional to $\bar{A}_{tree}$ and with a u-quark to $V_{ub}V_{us}^* = O(\lambda^4)$. Hence all penguin diagrams contribute with the same weak phase as the tree diagram, up to corrections of order $\lambda^4 \sim 10^{-3}$. The hadronic uncertainties are only of that order.

The CP eigenstate K_S^0 is formed from $K^0 - \bar{K}^0$ mixing. This mixing factor adds to the value of $\lambda_{J/\psi K_S^0}$. The participating amplitudes, V_{cs} and V_{cd} have no CP violating phase in the Wolfenstein parameterization up to order λ^4 and do not contribute to the imaginary part of $\lambda_{J/\psi K_S^0}$.

$\bar{A}_{tree}/A_{tree}$ is also real giving $\phi = 0$ and using 5.26,

$$\mathrm{Im}\lambda_{J/\psi K_S^0} = \sin(2\beta - 2\phi) = \sin(2\beta). \tag{5.29}$$

Detection of an asymmetry in the golden decay gives a direct measurement of $\sin(2\beta)$ of the unitary triangle with hadronic uncertainties of order 10^{-3}.

Some other B decays which can be used to measure the angles of the CKM unitary triangle are $B \to \pi\pi$, $B \to \phi K_S$, $B_s \to \rho K_S$.

Chapter 6

The $b\bar{b}$ Cross Section at HERA-B

6.1 Introduction

The estimates of the $b\bar{b}$ cross section at the HERA-B experiment as presented in the technical proposal [2] is based on theoretical predictions and comparisons with a limited number of experimental results (Figure 5 and 6 in [2]). The theoretical uncertainties range about a factor of two up or down, mainly due to the choice of the effective b-quark mass, the scale at which the strong coupling constant is evaluated and the parton distribution functions. Among the available data, the E789 fixed target experiment with a beam of 800 GeV protons is most relevant for the HERA-B case. This is also the measurement that falls nearest to the lower range in the predictions. The most recent differential cross section measured by the E789 experiment is [16], [17]

$$\frac{\mathrm{d}^2\sigma}{\mathrm{d}x_F \mathrm{d}p_T} = (107 \pm 28 \pm 19)\ \mathrm{pb}/GeV^2/\mathrm{nucleon}$$

for pN interactions at 800 GeV beam energy and at $x_F = 0.05$ and $p_T = 1$ GeV. The integrated b-quark production were obtained by extrapolation over all x_F and p_T:

$$\sigma(pN \to b\bar{b} + X) = (5.7 \pm 1.5 \pm 1.4)\ \mathrm{nb/nucleon}.$$

The E789 collaboration used a model to simulate b-quark production and fragmentation, that was checked to be consistent with PYTHIA Monte Carlo simulations [17].

The most pessimistic value of 6 nb given in the proposal [2] and design report [3] is based on an earlier, superseded calculation from the E789 collaboration [18]

$$\frac{\mathrm{d}^2\sigma}{\mathrm{d}x_F dp_T} = (159 \pm 44 \pm 25)\ \mathrm{pb}/GeV^2/\mathrm{nucleon},$$

which would imply a total cross section of about 7±2.5 nb at the HERA-B experiment.

6.2 Nuclear Dependence

In all cross section estimates, as well as in comparisons of data from experiments, a linear dependence on the mass number of the target nucleus is assumed. This relies on results from charmed meson, J/ψ and Υ production (table 5 in [2]). The observed suppression of J/ψ and Υ production could be caused by conversion to open charm or beauty pairs, through interaction with co-movers or with the nucleus. For D and B mesons this mechanism would be absent. The E789 experiment uses targets of gold and beryllium to measure the nuclear dependence of D-meson production by 800 GeV protons [19]. This has given a value 1.02±0.05 of the exponent in $\sigma(A) \propto A^\alpha$ at $0.0 < x_F < 0.08$, $< x_F >= 0.031$. At large x_F the momentum fraction of the target parton is small and may be influenced by shadowing of the gluon structure function. According to [19] this would at most cause a reduction in α for the total D cross section to 0.96. The WA82 experiment [22] has measured the nuclear dependence on D-meson production by 340 GeV pions over the entire phase space, resulting in the exponent α=0.92±0.05. At higher energies the dependence could be stronger.

The E789 measurement of the $\mathrm{b\bar{b}}$ cross section is made with a target of gold. In HERA-B much lighter targets are used, which implies that any nonlinear nuclear dependence would give reasons to estimate a higher cross section.

6.3 Feynman's x Distribution

The cross section is measured by E789 at $0 < x_F < 0.1$ and $p_T < 2$ GeV. The extrapolation to the entire phase space is nontrivial (fig 6.1).

The model used by E789 to integrate the cross section is based on the next-to-leading order calculations by Mangano, Nason and Ridolfi [20]. Fragmentation effects have also been taken into account by applying the Peterson function [21], which softens the x_F distribution. In hadronic production

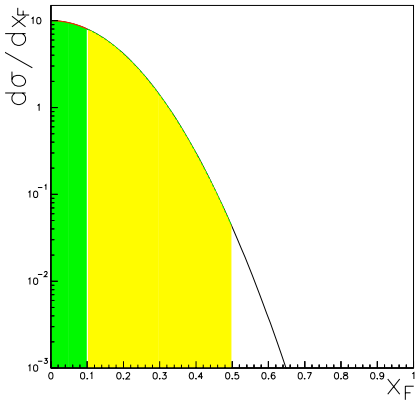

Figure 6.1: *Feynman's x distribution. The data point from E789 is at $x_F < 0.1$. The acceptance of the HERA-B detector extends out to x_F=0.5*

the fragmentation is expected to decrease the cross section by roughly 20%. Experimental results from D production show that the distribution is displaced to higher x_F, than expected from NLO+fragmentation functions. In pp and p-emulsion interactions [23], the measured distribution is, by chance, consistent with NLO calculations without fragmentation and in π-nucleon interactions [22] the distribution is even harder.

The physics models would agree on that the $b\bar{b}$ production should be integrated over phase space using NLO calculations with an overlayed fragmentation function, if additional nonperturbative effects can be neglected. However, if the deviations from NLO calculations plus the fragmentation function are consistent with those found in $c\bar{c}$-production, this assumption leads to an underestimate of the total $b\bar{b}$ production cross section. If the fragmentation and the nonperturbative hardening effects cancel exactly, as in D production, this underestimate is of the order of 20%. The same effects that increase the cross section under integration over x_F could decrease it under integration over p_T with a few percentages.

6.4 Summary

The total $b\bar{b}$ cross section from the E789 experiment was obtained by extrapolation from small x_F and p_T, to $\sigma(pN \to b\bar{b}+X) = 5.7 \pm 1.5 \pm 1.4$ nb/nucleon. Regarding the uncertainty in the nuclear dependence ($0.9 < \alpha \leq 1.0$) this revalues:

$$\sigma(pN \to b\bar{b} + X) \;=\; 6.0 \pm 1.6 \pm 1.7 \text{ nb/nucleon.}$$

The uncertainties in the Feynman's x distributions and the above argumentation indicate that this is an underestimate of up to 20%. Rescaling

10% and adding the uncertainty to the systematical error, the final estimate becomes

$$\sigma(pN \to b\bar{b} + X) \;=\; 6.6 \pm 1.7 \pm 2.2 \text{ nb/nucleon.} \qquad (6.1)$$

This means that the total cross section will be greater than 2.2 nb/nucleon with 95% C.L.

With an interaction frequency of 40 MHz, the estimated cross section corresponds to 20 B mesons produced per second in HERA-B.

Chapter 7

Analysis in HERA-B

7.1 Introduction

The main goal of the HERA-B experiment is to measure CP violation in the golden channel. Data taking with the full detector is scheduled for 1999. The preparations for data taking do not only include detector construction. The trigger processing and handling of data must be ready at the same time. All development is dependent on Monte Carlo simulations of a completed detector and its response to an event. The final reconstruction and analysis program will use the filtered data stored on tape to extract the physics parameters. To develop such a program a simulation of the events including a complete detector and a complete data processing is desired. The comparison of real data with a fully simulated event is necessary for the understanding of the results. The simulation must include every relevant detail of the chain.

The different parts of the simulation and reconstruction chain in HERA-B are described in this chapter. The full analysis of the golden channel include understanding of the golden decay, the background and the tagging of the flavour of the B meson. In this thesis the reconstruction of the golden decay is performed. The method is supposed to be applicable to simulated as well as real response from the complete detector.

7.2 HERA-B Software

Primary Interactions

The type of interaction in HERA-B is 820 GeV protons colliding on a nucleon. The order of 10 particles are produced per interaction. In 10^{-6} of the cases a $b\bar{b}$ pair is produced. The simulation of the HERA-B events is done in

the Analysis and Reconstruction Tool, ARTE [27]. ARTE is a frame for the offline programming and part of the online programming. The mechanism for heavy quark production in proton-nucleon collisions is simulated by PYTHIA 5.7 and JETSET 7.4 [24]. Interactions with nuclei are managed by FRITIOF [25], which is made compatible with PYTHIA 5.7. The HERA-B events are generated in two steps. Heavy hadrons from a $b\bar{b}$ pair generated by PYTHIA are saved and the rest of the event is produced using FRITIOF. For simulation of minimum bias interactions only FRITIOF is used.

PYTHIA simulates the mixing and decay of the neutral mesons. Care has to be taken to have one meson decaying golden and the other B hadron according to the particle decay table in [26].

The decays of long-lived particles are done during simulation of the detector response, outside PYTHIA and FRITIOF.

Detector Simulation

The hardware simulation is essentially divided into two parts. The geometry of the detectors and the physical response of the material on a moving particle are simulated by GEANT routines. The response of the readout is simulated in digitization routines and realistic information stored in banks to be used for online and offline analysis.

The implementation of the HERA-B detector into GEANT is handled by a program called HBGEAN [29]. It creates geometry structures for use in GEANT and ARTE and provides the digitization routines.

The target (fig. 3.1 and fig. 7.3) consists of two sets of four Aluminum ribbons at a distance of 5 σ from the beam and separated by $\sim$ 5 cm along the direction of the beam. The ribbons are 500 μm long and 50 μm thick.

The vertex vessel, containing the target and the vertex detectors, is implemented including a hole for the beam. The beampipe is a 500 μm thick aluminum tube.

Detailed information of the geometry of vertex and tracker planes are necessary for track reconstruction. The MC simulation of the Silicon Vertex Detector (SVD), the Outer Tracker Honeycomb Drift Chambers (HDC) and the inner tracker with a Microstrip Gaseous Chamber technique (MSGC) is consistent with the technical design report [3], although HDC does not yet have the exact modular structure as planned for the real detector.

Real measurements of the magnetic field exist [30] and can be used for the simulation. For the present analysis a homogeneous magnetic field parallel with the y axis is assumed. The radius of the field is 1.4 m and the strength is 8 kG.

The high-p_T trigger chambers, the TRD and the calorimeter (ECAL) are also described in detail. The muon system, needed to identify muons and improve the track parameters, is not yet used in the analysis. The RICH is included as material (a trapezoid of gas with glass in the front and end sides). Charged kaon identification is not needed for the reconstruction of the golden decay.

In the digitization, the response from a particle on each cell of various detector parts is calculated. In SVD and MSGC a coordinate is measured by detecting the center of gravity of a strip cluster. HDC gives the coordinate of the hit wire supplemented by the absolute value of the drift distance. In the digitization the efficiencies of the detector components are included. For HDC outer tracker this efficiency is 98% and for the MSGC inner tracker it is 95%.

Reconstruction

The tracks are reconstructed using a Kalman filtering technique [31]. Kalman filtering is a fast progressive fit adopting the least squares method. Energy loss in the detector material is accounted for as well as trajectory deflection due to multiple scattering in the Coulomb field of the nuclei. The ionization losses are assumed to be negligible. Electrons lose energy via electromagnetic radiation. Bremsstrahlung corrections are done for losses inside the magnet.

The RANGER program [31] provides pattern recognition and track reconstruction up to ECAL.

A full pattern recognition needs matching with SVD pattern recognition. Pattern recognition efficiencies in the pattern tracker is better than 96% for particles from the golden decay. In the present analysis this efficiency is applied explicitly and the tracks are reconstructed using ideal pattern recognition. The ideal pattern recognition option performs a fast track reconstruction, where hit assignment to tracks is taken from the Monte Carlo truth.

For vertex reconstruction a stand alone package [33] designed for HERA-B geometry is available and will be integrated into ARTE. The vertex package reconstructs vertices outside the magnetic field with or without mass constraints and from an arbitrary number of outgoing tracks. It does vertex pattern recognition and reconstructs main vertices on target wires.

Inside the magnetic field there is not yet a standard procedure for vertex fitting.

7.3 The Golden Channel

A reconstruction chain for the golden decay has been constructed using HERA-B simulation and analysis tools. Instructions for users are found in [35]. A description of the performance and the obtained results are presented here.

Trigger Simulation

Events with the golden decay have to be selected in an interaction rate of 10 MHz and the final state tracks found among $\sim$ 200 background tracks. The main trigger for this task is the J/ψ trigger described in chapter 3.4. Complementing di-lepton and high-p_T triggers will increase the total trigger efficiency by a couple of percents. In this analysis only the J/ψ trigger is studied. Awaiting a complete trigger simulation a fast check is carried out before the full track reconstruction on accepted events.

The trigger efficiency is dominated by the selection at the pretrigger level. Here two leptons of equal flavour must appear either as penetrations into the muon chamber or as high-energy electromagnetic showers in the calorimeter. At the first level trigger, these depositions are associated with track candidates. The geometrical acceptance of the MC tracks determines the pretrigger loss. Trigger leptons that go through all trigger layers reach also the calorimeter, respective the muon chambers. The first trigger step is therefore replaced by a requirement of hits in all trigger layers indicated in fig. 3.3. The identification of the particles are taken from the MC truth.

For this analysis the track parameters are obtained using a full track reconstruction. To be sure to study only tracks which are in the geometrical acceptance, some fiducial cuts are applied. In total more than 17 hits are required for a track. Only tracks with momenta higher than 1 GeV are accepted. The number of hits inside the magnet is required to be larger than 5. For electrons, the momentum resolution is sometimes still poor due to bremsstrahlung. Awaiting a bremsstrahlung correction method, a cut on dp/p^2 at 0.01 is applied to reject those events.

The HERA-B first level trigger cuts, on the lepton tracks from J/ψ candidates are then applied on the momenta, 5 GeV$< p <$200 GeV, and the transverse momenta, $p_T > 0.5$ GeV.

The cuts on the invariant mass around the J/ψ mass is currently placed at $2.75 < m_{J/\psi} < 3.50$ GeV. The correction for bremsstrahlung in front of the magnet is omitted in the analysis. To compensate for this the lower mass cut for electron pairs is placed at 2.0 GeV. The momenta and invariant mass distributions are depicted in fig. 7.1. The trigger steps are summarized in

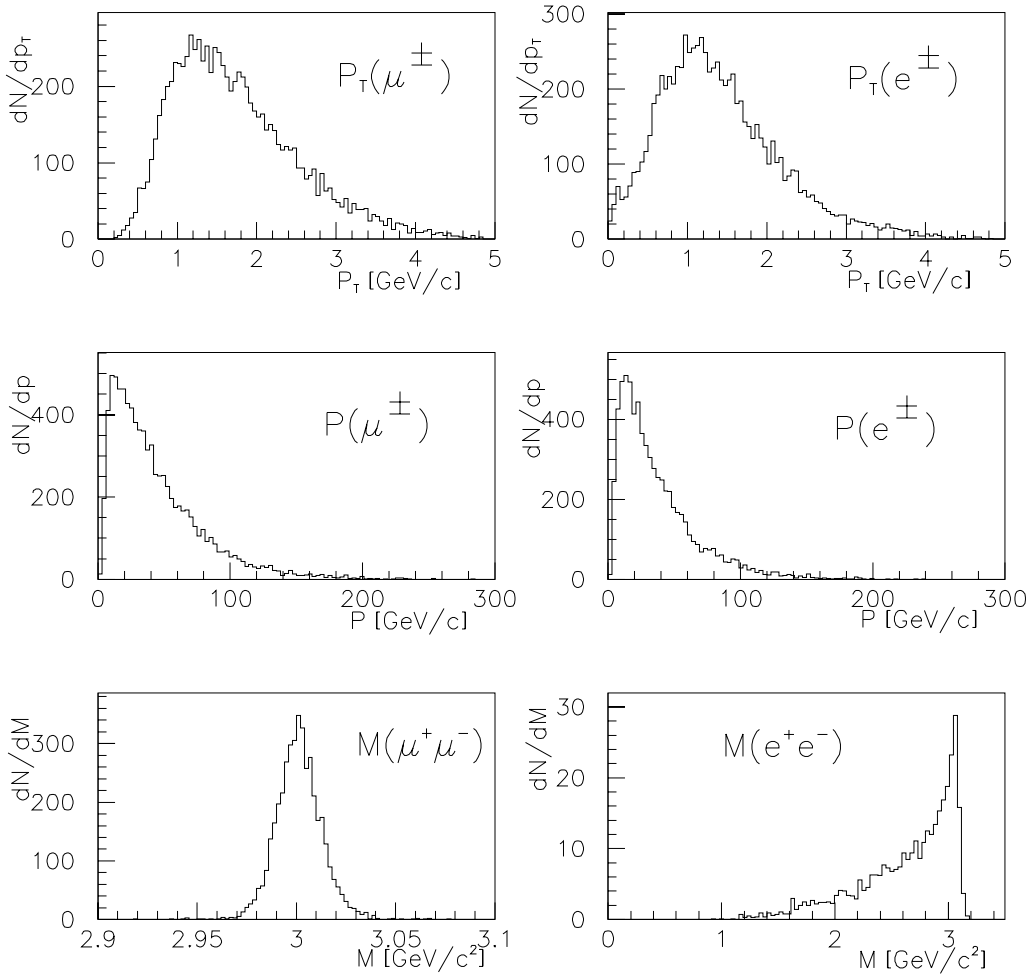

Figure 7.1: *The transverse momentum, momentum and invariant mass, distributions of muons respective electrons from the triggering J/ψ. The quantities are obtained using full track reconstruction.*

J/ψ Trigger Criteria	Efficiency	Proposal
Geometrical Acceptance	65%	70%
Muon pairs:		
momentum cuts	95%	92%
mass cut	$>$ 99%	99%
Electron pairs:		
momentum cuts	77%	51%
mass cut	90%	91%
track quality, dp/p^2	98%	

Table 7.1: *Trigger criteria and track reconstruction efficiencies obtained using HERA-B software of 1996. The cuts are strongly correlated. Comparison with numbers in the HERA-B proposal.*

table 7.1. The efficiencies obtained in this analysis are compared to the efficiencies which were calculated for the proposal [2]. Similar trigger efficiencies were obtained in [34], where track parameters were found simulating using first level trigger algorithms.

The total reconstruction efficiency is less dependent on the higher level trigger selections. Those criteria are incorporated in the overall analysis chain.

Golden Decay Reconstruction

Tracks on triggered events are reconstructed in the main tracking system using RANGER [31]. Pattern recognition is not included.

The real J/ψ events selected by the first level trigger will include all background J/ψ produced directly at the target wires as well as fake J/ψ from double semileptonic charm decays. The most efficient reduction of this background comes from a requirement of secondary vertex separation. A cut on the distance of the J/ψ from the target is applied already at the second level trigger. To increase statistical accuracy the secondary vertex criterion is considered only at the end of this analysis.

The J/ψ is finally accepted if the decay vertex can be fitted with a good χ^2 using routines from [33]. A cut is applied around the J/ψ mass. To compensate for bremsstrahlung losses, there is no lower limit for the electrons. With a proper bremsstrahlung correction a lower limit requirement will be possible.

For each selected J/ψ event the K^0_S candidates are picked out. The branching ratio of K^0_S to charged pions is 68.6% [26]. But only kaons decay-

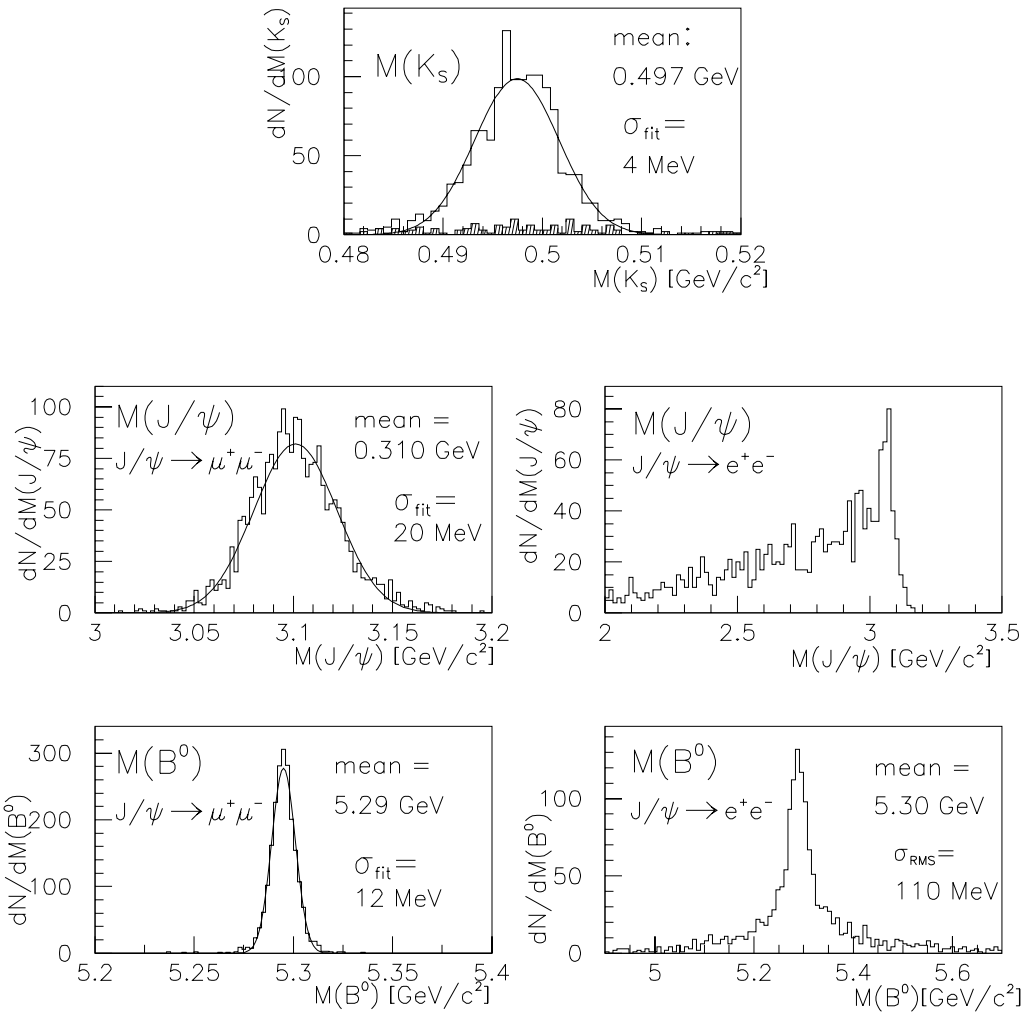

Figure 7.2: *The invariant masses of particles of reconstructed K^0_S, J/ψ and B^0. K^0_S reconstructed in the magnet are fitted with a Gaussian function. K^0_S reconstructed before the magnet are shown shaded in the plot. J/ψ and B^0 mass resolutions are represented for $J/\psi \to \mu^+\mu^-$ and $J/\psi \to e^+e^-$ respectively.*

ing before half of the magnet can be reconstructed. No particle identification is used to select pions. All combinations of particles from a common reconstructed vertex and with an invariant mass compatible with the K_S^0 mass are accepted.

14% of all K_S^0 decay inside the simulated magnetic field. In the real data analysis, vertex fitting algorithms have to be written to apply to an inhomogeneous field. For this analysis, routines from [32] for the simulated homogeneous field have been interfaced to arte and integrated into the strategy of the program. Seeds of track pairs of opposite charges at a reasonable distance (maximum of 1 cm at the closest approach) and with an invariant mass around the K_S^0 mass ($m_{K_S^0} \pm 0.5$ GeV) are accepted for a least square fit. The point of closest approach is required to be before or in the first half of the magnet (z $<$ 450 cm). The quality of the tracks is also checked: $dp/p^2 < 0.01$. The quality is correlated to the number of coordinates.

Candidate pairs with common vertices ($\chi^2 < 10$) and invariant masses $m_{\pi^+\pi^-} = m_{K_S^0} \pm 0.015$ GeV are accepted and the vertices fitted with a mass constraint on the K_S^0. The mass distribution of the reconstructed K_S^0 is shown in fig. 7.2.

The K_S^0 track parameters are obtained. Each K_S^0 candidate is fitted together with the J/ψ to form the secondary vertex of the B^0 meson. Since the decay length of the J/ψ is negligible ($\sim 10^{-10}$m), the B^0 decay vertex is reconstructed as a three particle vertex, with a mass constraint on the two leptons. The mass resolutions in fig. 7.2 of reconstructed J/ψ and B^0, where $J/\psi \to \mu^+\mu^-$, can be compared with the numbers in the HERA-B Design Report [3]: $\Delta M_{J/\psi} \approx 15$MeV, $\Delta M_{B^0} \approx 8$ MeV.

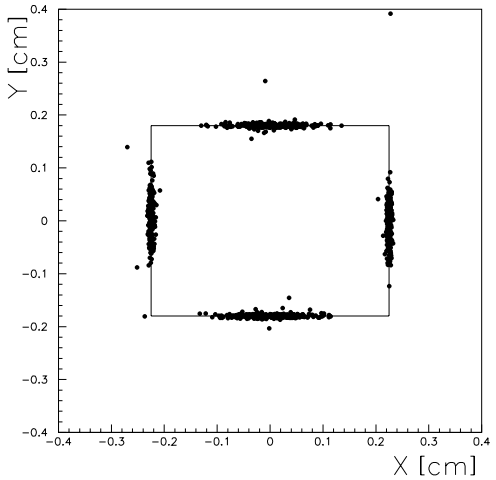

Figure 7.3: *Reconstructed golden B^0 mesons ($B^0 \to J/\psi K_S^0$), using HERA-B reconstruction tools. A scatter plot of the vertical coordinates of the tracks at the z-positions of the target wires. The lines show the Monte Carlo positions of the wires.*

B^0 candidates are accepted if the decay vertex is reconstructed ($\chi^2 < 15$) and the invariant mass is in the m_{B^0} range: $m_{\mu^+\mu^- K^0_S} = m_{B^0} \pm 30$ MeV for the muon channel and $m_{e^+e^- K^0_S} = m_{B^0} \pm 60$ MeV for the electron channel, to compensate for bremsstrahlung losses. The candidates are fitted with a mass constraint also on the B^0 mass. The B^0 is required to point to a target wire. This can be done in two ways:

1. All main vertices are reconstructed on the target wires. If the B^0 is compatible with one of them, this vertex is the primary vertex of the B^0. For golden B this works in 87% of the cases.

2. If the B^0 does not point to any of the main vertices, the distance to a target wire is computed and a primary vertex with the B^0 only, is reconstructed.

Reconstruction cuts	Efficiency	Proposal
Pion pairs:		
Geometrical Acceptance	60%	70%
K^0_S vertex, $\chi^2 < 10$ and $m_{K^0_S} \pm 15$ MeV	91%	97%
Muon pairs:		
J/ψ vertex, $\chi^2 < 10$ and $m_{J/\psi} \pm 60$ MeV	95%	$> 99\%$
B^0 decay vertex, $\chi^2 < 15$ and $m_{B^0} \pm 30$ MeV	93%	95%
B^0 primary vertex, $\chi^2 < 10$	$> 99\%$	$> 99\%$
Electron pairs:		
J/ψ vertex, $\chi^2 < 10$ and $0 < m_{J/\psi} < 60$ MeV	95%	$> 99\%$
B^0 decay vertex, $\chi^2 < 15$ and $m_{B^0} \pm 60$ MeV	59%	67%
B^0 primary vertex, $\chi^2 < 10$	96%	98%

Table 7.2: *Reconstruction efficiencies for the golden decay obtained using HERA-B software of 1996. Comparison with values computed for the HERA-B proposal [2].*

All B^0 decaying to $\mu^+\mu^- K^0_S$ and 97% of the $e^+e^- K^0_S$ decays point to a target

wire. With this last requirement fulfilled, the golden decay is reconstructed. The cuts and obtained efficiencies are summarized in table 7.2.

A measurement of the decay length of the B^0 meson is necessary for two reasons. It is needed to fit the time dependent asymmetry. It is also crucial in the reduction of background J/ψ. For the cut, the vertex separation is given as

$$V_{sep} = \frac{Z_{sec} - Z_{prim}}{\sigma_z}, \tag{7.1}$$

where Z_{sec} is the reconstructed z-coordinate of the decay vertex, σ_z is the variance of this coordinate. Z_{prim} is given at the high-z edge of the wire, where the B^0 was produced. Placing the cut at $V_{sep} > 8$ corresponds to a decay length of $\sim 0.7\ \tau_B$, see fig. 7.4.

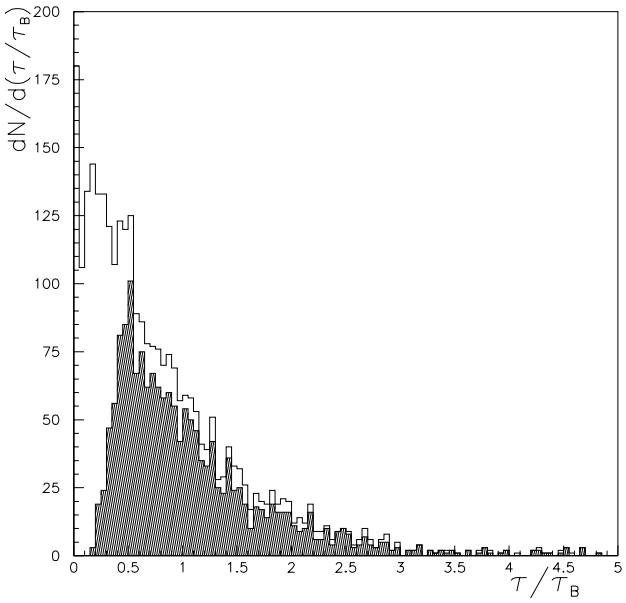

Figure 7.4: *The proper decay time of reconstructed B^0 before (empty) and after the vertex cut (shaded).*

Further background reductions can be obtained by cuts on the decay angles of the B^0 and the J/ψ (see fig. 7.5). The cuts are defined in the center of mass frame of the decaying particle. For correlated leptons of a triggered J/ψ, as well as for correlated K^0_S and a triggered J/ψ, the decay angles are large. Background particles are concentrated in the forward direction. The kinematic cuts are summarized in table 7.3.

To estimate the total efficiency for the golden decay, the particle identification and pattern recognition efficiencies are introduced explicitly. The total efficiencies are given in table 7.4 and compared with the proposal numbers.

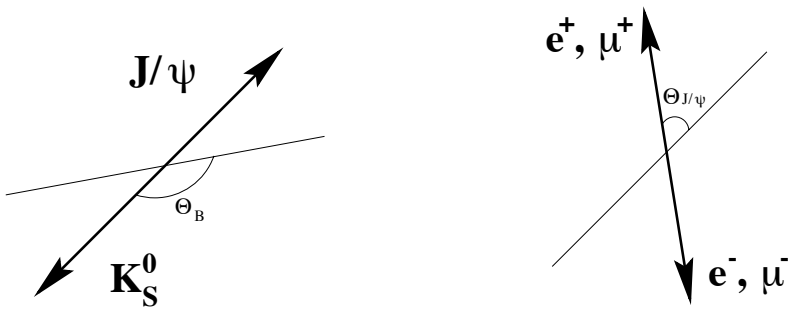

Figure 7.5: *The Golden Decay. Illustration of the decay angles in the rest frame of the decaying particle and with respect to its direction of flight in the lab system.*

Kinematic cuts	$(J/\psi \to \mu^+\mu^- K_S^0)$	$(J/\psi \to e^+e^- K_S^0)$
J/ψ decay angle, $\lvert\cos\theta_{J/\psi}\rvert < 0.7$	85%	86%
B^0 decay angle, $\lvert\cos\theta_B\rvert < 0.9$	94%	93%
Vertex separation $> 8\sigma$	69%	69%

Table 7.3: *Kinematic cuts for the golden decay, $B \to J/\psi K_S^0$. The reductions after the cuts are given separately for the decays $J/\psi \to \mu^+\mu^-$ and $J/\psi \to e^+e^-$.*

Summary	Efficiency		Proposal	
	$(J/\psi \to \mu^+\mu^-)$	$(J/\psi \to e^+e^-)$	$(J/\psi \to \mu^+\mu^-)$	$(J/\psi \to e^+e^-)$
Geometry, Trigger	62%	43%	61%	32%
Geometry pions	60%	60%	70%	70%
Reconstruction	86%	50%	91%	63%
Kinematic cuts	55%	55%	55%	55%
Pattern recognition	85%	85%	85%	85%
Particle ID	94%	85%	94%	85%
Total	14%	5%	17%	6%

Table 7.4: *Efficiencies for the Golden Decay reconstruction in the HERA-B experiment. Comparisons with numbers given in the HERA-B proposal [2].*

Background	$(J/\psi \rightarrow \mu^+\mu^-)$	$(J/\psi \rightarrow e^+e^-)$
Cross section	50	50
Branching ratios	$2 \cdot 10^{-3}$	$2 \cdot 10^{-3}$
Geometry, Trigger	0.56	0.39
Reconstruction	$8 \cdot 10^{-4}$	$3 \cdot 10^{-3}$
Pattern recogn.	0.92	0.92
Particle ID	0.94	0.85
Vertex cuts	$< 10^{-3}$	$< 10^{-3}$
Total	$< 4 \cdot 10^{-8}$	$< 1 \cdot 10^{-7}$

Table 7.5: *Reduction efficiencies for the background of J/ψ produced at the position of the target. The reduction efficiency for the vertex cut is cited from the proposal [2]. Note that the cuts on decay angles are omitted. The study was made on $\sim$ 2000 events, each with one $J/\psi \rightarrow \mu^+\mu^-$ and four Poisson distributed minimum bias inelastic events.*

Background

The reconstruction method is tested against the background of direct J/ψ produced at the target. This type of background is the least reduced by trigger and reconstruction cuts. It is nevertheless not the most difficult background, since the cross section "only" is a few thousand times larger ($\sigma_{J/\psi}$ = 300-400 nb/nucleon as compared to e.g the double semileptonic charm decay cross section 30 μb) and the decay cut is very effective in this case. The obtained reduction efficiency in table 7.5 is comparable with the number given in the proposal [2] for leptons from Charm events.

The most dangerous background is hadrons which are misidentified as muons, due to punch through in the muon chamber, and combined with any K^0_S to form a fake golden event. The total rate per year after all cuts would be less than 10^{-6} [2].

The ratio of background over signal is R < 0.35 for muons and R < 2 for the electron channel in the most pessimistic case. According to discussion in the proposal, the effectiveness of the vertex cut is underestimated and therefore the rejection factor is an underestimate. Further background studies may prove that the decay angle cuts are superfluous, which would increase the statistics with 20%.

Extracting CP Violation Measurement

The time dependent asymmetry in (5.27) is plotted and the CP measurement, $\sin 2\beta$, obtained from the fit. Remembering (5.28) and (5.29), the asymmetry is

$$a(t) = \sin 2\beta \ \sin xt \ , \tag{7.2}$$

with $t = \gamma \cdot \tau_B, \ \ \gamma = E_B/m_B$. For linear fitting (see e.g [36]) the error on the parameter, $\sin 2\beta$, is given as

$$\sigma^2_{\sin 2\beta} = \frac{1}{\sum_i \frac{(\sin xt_i)^2}{\sigma_i^2}} \ .$$

in the case of perfect tagging.

For asymmetry measurements, when the asymmetry is small, it holds that

$$\sigma = \frac{1}{\sqrt{n}} \ , \tag{7.3}$$

where n is the total number of events in the sample. This gives

$$\sigma^2_{\sin 2\beta} = \frac{1}{\sum_i n_i \sin^2 xt_i} \ , \qquad n_i = N(t=0)e^{-t_i} \tag{7.4}$$

The summation is replaced by an integral giving the statistical error

$$\Delta \sin 2\beta \approx \frac{1}{\sqrt{N(0)}} \cdot \frac{1}{\left(\int_{t_0}^{\infty} e^{-t} \sin^2 xt \ \mathrm{d}t\right)^{\frac{1}{2}}} = \frac{1}{\sqrt{N(t_0)}} \cdot \frac{1}{M(t_0)} \ , \tag{7.5}$$

with

$$M(t_0) = \left(\frac{1 + 4x^2 - \cos 2xt_0 + 2x \sin 2xt_0}{2(1+4x^2)}\right)^{\frac{1}{2}} . \tag{7.6}$$

M grows with the decay time cut t_0, reflecting how the asymmetry builds up slowly.

In order to determine the best choice of t_0, look at the part of the error, which is dependent on the cut.

$$F(t_0) = \frac{1}{\sqrt{e^{-t_0}}} \cdot \frac{1}{M(t_0)} \ . \tag{7.7}$$

This function stays flat for t_0 up to about 0.7 τ_B (as seen in fig. 7.6), which is where the cut has been placed in the analysis. The interpretation of the curve is that the asymmetry at $t < 0.7$ is so low that those extra events would hardly increase the accuracy of the measurement. The accuracy of a time integrated asymmetry would even decrease without the cut.

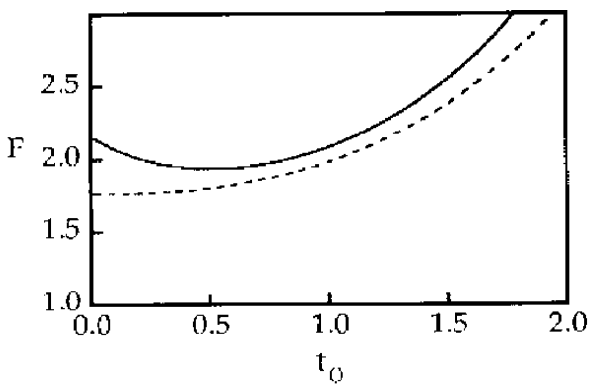

Figure 7.6: *Coefficient $F(t_0)$ governing the dependence of ΔA_{CP} on the decay time cut, for a fixed total number of events. Top line: time-integrated asymmetry, bottom: fit to the time-dependent asymmetry. From [2].*

The statistical factor from the fit is represented as $K = 1/M^2(t_0)$. With the decay time cut at 8σ, the statistical factor has been calculated in the analysis to be

$$K = 2.3 \ , \tag{7.8}$$

which corresponds to $t_0 = 0.7\tau_B$. Without a cut on the target-vertex separation, $K_0 \approx 3.1$.

Additional sources of errors arise in determining the initial flavour of the decaying B meson. The most powerful method is to reconstruct decays of the second B hadron in the event. The sign of the charge of a soft pion accompanying the B meson under investigation could also serve as a tag. The methods and tagging powers are summarized in table 7.3. Two effects dilute the tagging:

- Mixing of the tagging B.
- Wrong tags due to particle misidentification, non-B tracks and ambiguous signatures etc.

The effect of dilutions and the probability to find a tag are defined as the tagging power. The study for the proposal give at hand the combined tagging power of the different methods:

$$P = 0.31 \ . \tag{7.9}$$

The total error on the CP asymmetry is now

$$\Delta \sin 2\beta \approx \frac{1}{P}\sqrt{\frac{K}{N_{t_0}}} \ . \tag{7.10}$$

TAG	METHOD	POWER
Lepton tag:	The sign of a high p_T lepton, which can be associated with the second B meson in the interaction.	0.17
Kaon tag:	The sign of a kaon, which can be associated with the second B meson in the interaction.	0.24
Charge tag:	Counting the charges of secondary vertex tracks, weighted by the momentum, since hard tracks are more strongly correlated in charge to the fragmenting quark.	0.16
Soft Pion:	The sign of a soft pion either from the decay of an excited B^{**} meson into the B under investigation, or from the local charge conservation in the quark fragmentation process.	Not studied

Using the central value of the cross section from chapter 6, and (3.4) and assuming an interaction rate of 40 MHz, the number of golden decays produced in a nominal year ($= 10^7$s) is 5300. 14% respective 5% in the muon and electron channels are reconstructed. This would give the precision of the measurement

$$\Delta \sin 2\beta \approx 0.218 \text{ after one year .} \tag{7.11}$$

In the case that background can not be completely neglected, the factor $\sqrt{1+R}$ is to be multiplied with the statistical error. According to the proposal the vertex cut is expected to clean the muon channel. For the electron channel the background might be in the 10% range. Taking this into account, this leads to

$$\Delta \sin 2\beta = 0.221 \text{ after one year ,} \tag{7.12}$$

which corresponds to 0.11 in four years. The systematic error is estimated to be less than 0.05 [2].

Chapter 8

Conclusion

The CP reach in the HERA-B experiment depends on some unknown factors:

- The size of the CP violating parameter, $\sin 2\beta$.
- The $b\bar{b}$ cross section at HERA-B kinematics.
- The hardware. The study is made for detectors with resolutions and efficiencies as given in [3].
- Reconstruction efficiencies including e.g bremsstrahlung corrections, pattern recognition and particle identification. Background studies show that looser cuts can be acceptable, which would increase the statistics.

The most crucial point is the large uncertainty in the $b\bar{b}$ cross section. To find the capabilities of the experiment, integration is performed over the cross section range in (6.1).

For each magnitude of the cross section, a t standard deviation measurement can be made for $\sin 2\beta > t \cdot \Delta \sin 2\beta$.

Considering the allowed region in the $\sin 2\beta$ parameter space and assuming equal probabilities for the central region (5.16), the probability for $\sin 2\beta$ to be in this range is

$$\mathrm{MIN}\left(1,\ \frac{(\sin 2\beta)_{max} - t \cdot \Delta \sin 2\beta}{(\sin 2\beta)_{max} - (\sin 2\beta)_{min}}\right).$$

Multiplying this probability function with the normal distribution around the expected $b\bar{b}$ cross section and integrating, the probability to measure $\sin(2\beta)$ with three standard deviations is 59% in one year of running and 93% in four years of running. The probability for a 4σ measurement is 33% in one year and 85% in four years.

Appendix A

$B^0 - \bar{B}^0$ mixing

The contents in this appendix is based on [13].

Neutral mesons like B^0 and $\bar{B}^0$ mix via an intermediate state. Any arbitrary state is a superposition of the flavour eigenstates, which obeys the time-dependent Schrödinger equation

$$i\frac{\mathrm{d}}{\mathrm{d}t}\begin{pmatrix} a \\ b \end{pmatrix} = \mathbf{H}\begin{pmatrix} a \\ b \end{pmatrix} = \left(\mathbf{M} - \frac{i}{2}\mathbf{\Gamma}\right)\begin{pmatrix} a \\ b \end{pmatrix}. \tag{A.1}$$

The eigenvectors are the mass eigenstates

$$\begin{aligned} |B_H\rangle &= p|B_0\rangle - q\left|\bar{B}^0\right\rangle, \\ |B_L\rangle &= p|B_0\rangle + q\left|\bar{B}^0\right\rangle; \quad |p^2| + |q^2| = 1. \end{aligned} \tag{A.2}$$

Studying CP violation, the ratio q/p is of interest:

$$\left(\frac{q}{p}\right)_B = \frac{M_{12}^* - \frac{i}{2}\Gamma_{12}^*}{M_{12} - \frac{i}{2}\Gamma_{12}}. \tag{A.3}$$

The width difference between the physical states is negligible compared to the mass difference:

$$\frac{|\Delta\Gamma_B|}{\Delta m_B} < 10^{-2}. \tag{A.4}$$

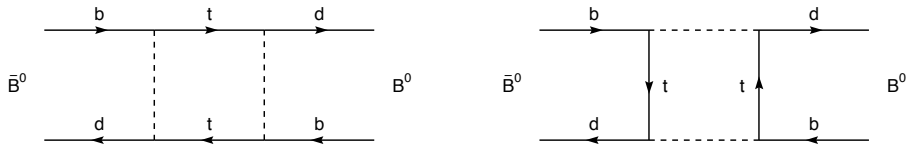

Figure A.1: $B^0 - \bar{B}^0$ *mixing.*

It follows that $|\Gamma_{12}| \ll |M_{12}|$ and the ratio can be approximated as

$$\left(\frac{q}{p}\right)_B \simeq -\frac{M_{12}^*}{|M_{12}|}\left(1 - \frac{1}{2}\mathrm{Im}\frac{\Gamma_{12}}{M_{12}}\right).$$

To order 10^{-2} the rate of $B^0 - \bar{B}^0$ mixing is just a phase, i.e

$$\left|\frac{q}{p}\right| \simeq 1. \tag{A.5}$$

In the Standard Model, the vertices in the box diagrams of fig. A.1 are responsible for the non-diagonal element M_{12}^* of the mass matrix. The contributions of the light c and u quarks can be neglected. The vertices can be expressed in terms of the CKM parameters:

$$\left(\frac{q}{p}\right)_B \simeq -\frac{M_{12}^*}{|M_{12}|} = \frac{(V_{tb}^* V_{td})^2}{|V_{tb}^* V_{td}|^2} = \frac{V_{tb}^* V_{td}}{V_{tb} V_{td}^*} = e^{-2i\beta}, \tag{A.6}$$

where β is one of the angles in the famous unitary triangle.

Consider the decay of neutral mesons into CP eigenstates,

$$A = \left\langle f_{CP}|\mathcal{H}|B^0\right\rangle, \quad \bar{A} = \left\langle f_{CP}|\mathcal{H}|\bar{B}^0\right\rangle. \tag{A.7}$$

The product

$$\lambda = \frac{q}{p} \cdot \frac{\bar{A}}{A} \tag{A.8}$$

is physically meaningful and is of interest in studies on CP violation. The measurable asymmetry in such studies is the difference in the number of B^0 and $\bar{B}^0$ decays after some time allowing for mixing.

$$a_{f_{CP}} = \frac{\Gamma(B^0(t) \to f_{CP}) - \Gamma(\bar{B}^0(t) \to f_{CP})}{\Gamma(B^0(t) \to f_{CP}) + \Gamma(\bar{B}^0(t) \to f_{CP})} \tag{A.9}$$

This asymmetry can be calculated in terms of λ. From (A.2),

$$\begin{aligned} |B^0(0)\rangle &= \tfrac{1}{2p}\left(|B_H\rangle + |B_L\rangle\right), \\ \left|\bar{B}^0(0)\right\rangle &= \tfrac{1}{2q}\left(|B_H\rangle - |B_L\rangle\right). \end{aligned} \tag{A.10}$$

The time evolution of the mass eigenstates are given by (A.1):

$$\begin{aligned} |B_H(t)\rangle &= e^{-iM_H t} e^{-\frac{1}{2}\Gamma_H t}\,|B_H\rangle\,, \\ |B_L(t)\rangle &= e^{-iM_L t} e^{-\frac{1}{2}\Gamma_L t}\,|B_L\rangle\,, \end{aligned} \tag{A.11}$$

where $M_i - \frac{i}{2}\Gamma_i$ are the eigenvalues. Using (A.4), $\Gamma_H = \Gamma_L$ and $\mathrm{M}_H = m_B + \Delta m_B$, $\mathrm{M}_L = m_B - \Delta m_B$.

$$\begin{aligned} |B^0(t)\rangle &= \tfrac{1}{2p} e^{-im_B t} e^{-\frac{1}{2}\Gamma_B t} \left[e^{-\frac{i}{2}\Delta m_B t} |B_H\rangle + e^{\frac{i}{2}\Delta m_B t} |B_L\rangle \right] \\ &= e^{-im_B t} e^{-\frac{1}{2}\Gamma_B t} \left[\cos\left(\tfrac{1}{2}\Delta m_B t\right) |B^0\rangle + i\tfrac{q}{p} \sin\left(\tfrac{1}{2}\Delta m_B t\right) |B^0\rangle \right] \end{aligned}$$

The amplitude of the decay of this B to the final state f_{CP} is

$$\begin{aligned} \langle f_{CP}|\mathcal{H}|B^0(t)\rangle &= e^{-im_B t} e^{-\frac{1}{2}\Gamma_B t} \left[A \cos\left(\tfrac{1}{2}\Delta m_B t\right) |B^0\rangle + i\bar{A}\tfrac{q}{p} \sin\left(\tfrac{1}{2}\Delta m_B t\right) \right] \\ &= A e^{-im_B t} e^{-\frac{1}{2}\Gamma_B t} \left[\cos\left(\tfrac{1}{2}\Delta m_B t\right) |B^0\rangle + i\lambda \sin\left(\tfrac{1}{2}\Delta m_B t\right) \right] \end{aligned}$$

The width

$$\Gamma(B^0(t) \to f_{CP}) = \; |A|^2 e^{-\Gamma_B t} \left[\tfrac{1+|\lambda|^2}{2} + \tfrac{1-|\lambda|^2}{2} \cos(\Delta m_B t) - \mathrm{Im}\lambda \sin(\Delta m_B t) \right]. \tag{A.12}$$

In a similar way, the corresponding width for $\bar{B}^0(t)$ is

$$\Gamma(\bar{B}^0(t) \to f_{CP}) = \; |A|^2 e^{-\Gamma_B t} \left[\tfrac{1+|\lambda|^2}{2} - \tfrac{1-|\lambda|^2}{2} \cos(\Delta m_B t) + \mathrm{Im}\lambda \sin(\Delta m_B t) \right]. \tag{A.13}$$

Using (A.5), (A.12) and (A.13), the measurable asymmetry in (A.9) is calculated as

$$a_{f_{CP}} \simeq \frac{(1-|\lambda|^2)\cos(\Delta m_B t) - 2\mathrm{Im}\lambda \sin(\Delta m_B t)}{1+|\lambda|^2}. \tag{A.14}$$

For many B decays it also holds that $|\mathrm{A}/\bar{\mathrm{A}}| \simeq 1$, so that $|\lambda| \simeq 1$ and

$$a_{f_{CP}} \simeq \mathrm{Im}\lambda \sin(\Delta m_B t). \tag{A.15}$$

This is a useful result, since it shows that the CP violating parameters in the Standard Model can be accessed in rather direct ways in the B system and without large hadronic uncertainties.

Bibliography

[1] The ATLAS collaboration, *ATLAS technical proposal*, Technical Report, **CERN/LHCC/94-43** (1994).

[2] T.Lohse et al., *An Experiment to Study CP Violation in the B System Using an Internal Target at the HERA Proton Ring*, Proposal, **DESY-PRC 94/02** (1994).

[3] The HERA-B collaboration, *An Experiment to Study CP Violation in the B System Using an Internal Target at the HERA Proton Ring*, Design Report, **DESY-PRC 95/01** (1995).

[4] X. Artru, G.B. Yodh, and G. Mennessier. *Practical theory of the multilayered transition radiation detector*, **Physical Review D**, 12(5):1289–1306, 1975.

[5] L. Fayard, editor. *Transition Radiation*, volume LAL-88-55, November 1988. Lectures given at l'Ecole Joliot Curie 1988, Carcans, France, September 26-30, 1988.

[6] Boris Dolgoshein. *Transition radiation detectors and particle identification*, Nuclear Instruments and Methods in Physics Research, A252:137–144, 1986.

[7] Boris Dolgoshein. *Transition radiation detectors*, Nuclear Instruments and Methods in Physics Research, A326:434–469, 1993.

[8] ATLAS Collaboration, *progress report on ATLAS milestones.* CERN/LHCC/94-22

[9] H. Danielsson et al., *A Modular Structure for the barrel TRT.* Technical Note CERN TA1/94-31, LUNFD6(NFFL-7100)1995.

[10] A.V.Berezhnoy, A.K.Likhoded, M.V.Shevlyagin, *Hadronic production of B_c-mesons*, **IHEP 94-48.**

S.S:Gershtein, V.V.Kiselev, A.K.Likhoded, A.V.Tkabladze, *Physics of B_c mesons*, **IHEP 94-81.**
V.V.Kiselev, A.K.Likhoded, Private communication.
A.V. Berezhnoi, V.V. Kiselev, A.K. Likhoded, A.I. Onishchenko *B(C) MESON AT LHC*,IFVE-97-2, Jan 1997. 27pp.

[11] K.Kolodziej, A.Leike, R.Rückl, *Production of B_c mesons in hadronic collisions*, **Physics Letters B 355** (1995) 337-344.

[12] M. Neubert *Heavy-Quark Symmetry*, **Physics Reports 245** (1994) 259-395.

[13] M. Neubert *B Decays and CP Violation*, **CERN-TH/96-55**, (to appear in International Journal of Modern Physics A).

[14] C. Jarlskog, in: *CP Violation*, edited by C. Jarlskog. World Scientific, Singapore, 1989.

[15] A. Gocksch *Strong CP Violation: The Neutron Electric Dipole Moment in Lattice QCD*, Madrid EPS HEP 1989:368-370.

[16] D.M. Jansen et al., *Measurement of the Bottom-Quark Production Cross Section in 800 GeV/c Proton-Gold Collisions*, **FERMILAB-Pub-94/403** (1994).

[17] D.M. Kaplan, *B Cross Section from E789*, **IIT-HEP-94-2** (1994).

[18] M. Schub, E789 Collaboration, *Charm and Beauty Production from Fermilab Experiment 789*, presented at the 28th Rencontre de Moriond, QCD and High Energy Hadronic Interactions, Les Arcs, France (1994).

[19] M.J. Leitch et al., *Nuclear Dependence of Neutral D-Meson Production by 800 GeV/c Protons*, **FERMILAB-Pub-94/012-E** (1994).

[20] M.Mangano, P.Nason, G.Ridolfi, **Nucl. Phys. B405**, 507 (1993).

[21] C.Peterson et al., **Phys. Rev. D 27**, 105 (1983).

[22] M.Adamovich et al., **Phys. Lett. B305** (1993) 402-406.
G.A.Alves et al., **Phys. Rev. Lett. 72** (1994) 812.

[23] K.Kodama et al. **Phys. Lett B263** (1991) 573-578.
R.Ammar et al., **Phys. Rev. Lett. 61:2185** (1988).

[24] CERN, Theory division. PYTHIA *5.6 and* JETSET *7.3 Physics and Manual*, **CERN-TH 6488/92**, September 1992.

[25] Hong Pi. *An Event Generator for Interactions between Hadrons and Nuclei* - FRITIOF *Version 7.* Submitted to Computer Physics Communication.

[26] Particle Data Group. *Review of Particle Properties* **Physical Review D50**, 1173 (1994).

[27] H. Albrecht et al. *ARTE. The Event Reconstruction and Analysis Tool for HERA-B*, **March 12, 1996.**
(http://www-hera-b.desy.de/subgroup/software/arte/arte_manual.ps)

[28] CN division Application Software Group. *GEANT Detector Description and Simulation Tool.* CERN.

[29] S. Nowak HBGEAN **HERA-B 94-123**, 1994
(URL: http://www-hera-b.desy.de/subgroup/software/hbgean.html).

[30] S. Spiridonov *Magnet measurement Analysis*, **HERA-B 96-141**, 1996.

[31] R. Mankel *Application of the Kalman Filter Technique in the HERA-B Track Reconstruction*, **HERA-B 95-239**.

R. Mankel *ranger - a Pattern Recognition Tool for the HERA-B Main Tracking System -Quick Introduction*, **February 12, 1997**
(http://www-hera-b.desy.de/subgroup/software/ranger−quick.ps).

[32] A. Spiridonov , R. Mankel, S. Nowak K^0_S *Reconstruction Performance*, **HERA-B 94-058.**

[33] T. Lohse *Vertex Reconstruction and Fitting*, **HERA-B 95-013.**

[34] M. Leuthold *Untersuchungen zur Effizienz der Rekonstruktion des Zerfalls* $B^0 \rightarrow J/\psi K^0_S \rightarrow \ell^+\ell^-\pi^+\pi^-$ *im HERA-B-Experiment anhand vollständig simulierter Modellereignisse*, Diplomarbeit, Institut für Physik, Mathematisch-Naturwissenschaftliche Fakultät, Humboldt-Universität zu Berlin, 1997.

[35] J. Ivarsson *Reconstruction Chain for the Golden Decay*, **HERA-B 96-267.**

J. Ivarsson *First Analysis Experience with HERA-B Simulation and Reconstruction Tools*, **HERA-B 95-226.**

[36] W. R. LEO *Experimental techniques in Nuclear and Particle physics.*